Enzyme-Mediated Multiphase Precipitation (EMMP): An Innovative Strategy for Ecotoxic Metal Immobilization in Aqueous Systems

Dickinson, Heloisa[a]; MacDonald, John[a]; Toney, Jaime L.[a]

[a] *College of Sciences and Engineering, School of Geographical and Earth Sciences, University of Glasgow*

Corresponding author: h.dickinson.2@research.gla.ac.uk

Co-authors: Jaime.Toney@glasgow.ac.uk

John.MacDonald.3@glasgow.ac.uk

Enzyme-Mediated Multiphase Precipitation (EMMP): An Innovative Strategy for Ecotoxic Metal Immobilization in Aqueous Systems

Dickinson, Heloisa[a]; MacDonald, John[a]; Toney, Jaime L.[a]

[a] *College of Sciences and Engineering, School of Geographical and Earth Sciences, University of Glasgow*

- Enzyme-mediated multiphase precipitation was applied for ecotoxic metals immobilization in water
- Immobilisation efficiency was above 95% for Pb^{2+}, Cd^{2+}, and Li^{+}
- Multiple mineral phases formed, including calcite, struvite and apatite
- Mitigation mechanisms included precipitation, adsorption, and biomolecular complexation
- EMMP remained effective under mildly acidic conditions (pH ~5.0)
- Waste-derived materials enabled low-cost, multifunctional remediation

Abstract

Ecotoxic metal contamination in wastewater and soil poses a critical environmental challenge due to its persistence, toxicity, and bioaccumulation potential. While conventional biogeotechnical methods like Enzyme-Induced Carbonate Precipitation (EICP) and Microbial Induced Carbonate Precipitation (MICP) have shown promise for metal immobilisation, their application is limited by excessive ammonium byproduct generation. In this paper, we present Enzyme-Mediated Multiphase Precipitation (EMMP), a novel approach that significantly reduces ammonium production while utilising waste-derived materials (i.e., soybean crude urease extract, bone meal and urea) to achieve simultaneous precipitation of metal-magnesium ammonium phosphates, carbonates, and calcium phosphates. We evaluated EMMP's effectiveness in removing nine metals (As, Cd, Co, Cr, Cu, Li, Ni, Pb, Zn) at three concentrations (2 mM, 5 mM, 20 mM). The process achieved removal efficiencies exceeding 95% for Pb, Cd, and Zn and 80% for Co, Ni, and Li through combined mechanisms of direct precipitation, co-precipitation, surface adsorption, and biomolecule-mediated interactions. Crystallographic analysis revealed calcite and struvite as primary mineral phases with distinct metal-dependent morphological variations. Relative to control conditions (defined as 100% ammonium production), EMMP reduced ammonium generation to below 5% for Cr, Cu, Pb, and As, to 20-45% for Ni, Co, and Cd, and maintained levels at 78-82% for Li and Zn. By integrating waste-derived materials and minimising ammonium generation, EMMP demonstrates an efficient, sustainable approach for metal remediation in aqueous environments, aligning with circular economy principles.

Graphical Abstract

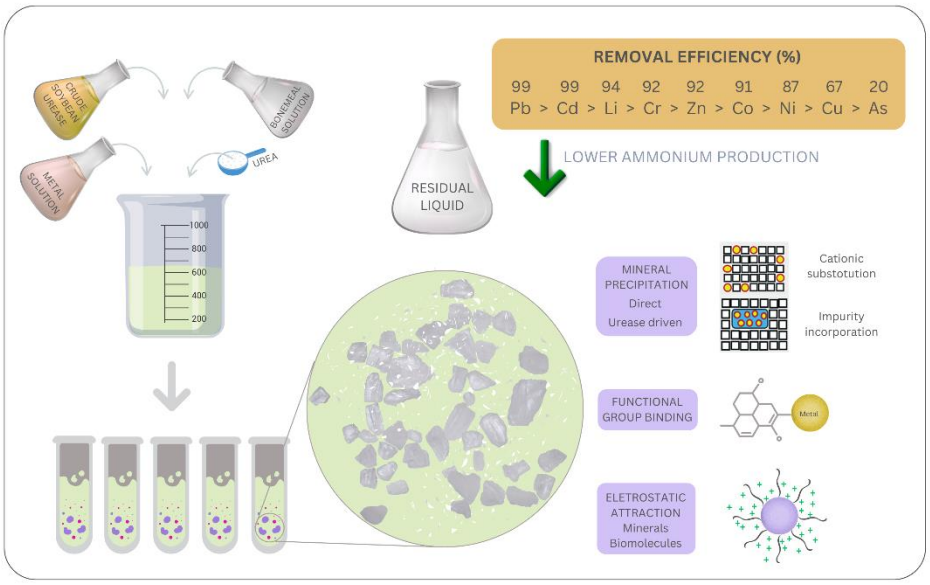

1. Introduction

Anthropogenic ecotoxic metals (EMs) contamination in water and soil is a major environmental issue in many urban areas. This increased concentration of EMs in soil and groundwater is not merely a significant public health matter but is also responsible for hindering ecosystem services such as nutrient cycling, soil fertility and carbon sequestration that are indispensable in a liveable city (IPCC, 2022). Sustainable land-use practices, pollution remediation and prevention, and conservation efforts that consider soil and groundwater are essential for maintaining the health and functionality of these vital ecosystems. Protecting soil and groundwater ecosystem services is necessary to guarantee water and food security, ecological health, and resilience to environmental change (UN, 2021).

Given the need for effective strategies to mitigate EMs contamination and restore ecosystem services, innovative biogeotechnical approaches have been explored for wastewater and soil remediation and stabilisation. Among these, Microbial Induced Carbonate Precipitation (MICP) and Enzyme Induced Carbonate Precipitation (EICP) have gained attention as sustainable techniques with the potential to immobilise EMs and simultaneously sequester carbon dioxide from the atmosphere or waste sources (Almajed et al., 2020; Xie et al., 2023; Bian et al., 2024; Wang et al., 2023). MICP and EICP rely on urease enzymes produced by ureolytic microorganisms or directly extracted from plants or organisms to catalyse the hydrolysis of urea into ammonia and carbon dioxide, leading to the precipitation of calcium carbonate ($CaCO_3$). The enzymatic and microbial processes that induce carbonate precipitation can also be leveraged to immobilise and sequester contaminants in wastewater and the soil matrix (DeJong et al., 2010). Both techniques proved to be efficient in immobilising inorganic contaminants predominantly through mechanisms of direct precipitation, co-precipitation, adsorption and surface complexation in

distinct environmental contexts, such as groundwater and wastewater (Torres-Aravena et al., 2018; Zheng et al., 2023; Zeng et al., 2025), soil improvement and erosion control (Gomez et al., 2015; Almajed, 2017; Arab et al., 2021; Moghal et al, 2020) and mining waste (Makinda et al., 2023; Ma et al, 1995). However, the ureolytic precipitation of carbonates generates substantial amounts of ammonium, which transforms into ammonia through pH-dependent equilibrium and can lead to environmental issues such as eutrophication, bio-toxicity, soil acidification, and formation of inorganic secondary particulate matter (Behera et al., 2010; Park et al., 2021).

Several methods have been proposed for the remediation of ammonium, such as ion exchange, struvite ($(NH_4)MgPO_4 \cdot 6H_2O$) precipitation, nitrification/denitrification, and adsorption (Gowthaman et al., 2022; Nagarajan et al., 2024; Farghali et al., 2024). Combining methods can often yield the best results, leveraging the strengths of each method to effectively manage and remove ammonium byproducts from MICP and EICP processes applied in soil and water. A significant challenge lies in the fact that once released into the environment, ammonium tends to be chemically adsorbed in the clay minerals or organic matter of the soils; it can also be dispersed through water systems or be transformed into gas ammonia, depending on the pH of the media. Managing and mitigating the dispersion of ammonium [NH_4^+] and its transformation into ammonia [NH_3] in the environment requires a strategic approach that involves containment and treatment. Although proven effective for ammonium remediation, the cited methods - combined or individually - constitute independent secondary treatment strategies that introduce additional steps to the initial remediation process, increasing both process complexity and operational costs. Selecting the appropriate method, or combination of methods, depends on factors such as the scale of the project, local environmental conditions, and specific site requirements while evaluating their economic feasibility and environmental trade-offs through Life Cycle Assessment (LCA) can provide crucial insights into their long-term sustainability and cost-effectiveness.

In light of these challenges, alternative approaches that address soil remediation and ammonium management in a single process have emerged. Phosphate precipitation mediated by enzymes or microbial activity is a dynamic and potent method for remediating contaminated soils and water, particularly in environments polluted by heavy metals and radionuclides, with reported remediation rates above 95% (Jiang et al., 2020; Han et al., 2022). The precipitation of phosphates induced by ureolytic processes has two important additional benefits when compared to EICP and MICP: 1) some of the precipitated phosphate phases like struvite and brushite can sequester the ammonium byproduct via mechanisms of precipitation and adsorption, and 2) due to general lower solubility, phosphates demonstrate better performance in stabilising heavy metals compared to carbonates, particularly for Pb and Zn, remaining immobilised in a broader range of pH, even in more acidic conditions (Jiang et al., 2020, Zeng et al., 2017).

In this study, we investigated the efficiency of Enzyme-Mediated Multiphase Precipitation (EMMP), a novel technique inspired by EICP and phosphate precipitation techniques that generate less ammonium byproduct than conventional EICP methods during Ems immobilisation. EMMP uses plant-derived urease crude extract, bone meal, and urea to precipitate carbonates, calcium phosphate compounds (CPCs) and metal-magnesium ammonium phosphates (M-struvite species) in just one stage.

We propose the use of local waste materials in a "waste-to-resource" approach and optimise the method based on life cycle assessment and greenhouse gas (GHG) protocol principles to decrease the consumption of non-renewable goods, GHG emissions and overall environmental impact and costs. This approach was employed to evaluate how EMMP's effectiveness in immobilising EMs and ammonium through immobilisation within the precipitated phases varies across nine specific metals – Cd, Co, Cu, Cr, As, Li, Ni, Pb and Zn. Additionally, by looking at the underlying mechanisms behind the variations in heavy metal immobilisation and residual levels of ammonium, we aim to demonstrate how incorporating waste-derived materials can maintain the same efficiency level as commercially available products while enhancing the sustainability of EMMP.

To assess the efficiency of EMMP in decreasing the concentration of EMs in water, we performed a series of test tube experiments with three different concentrations of EMs individually. Single Crystal X-ray diffraction (SC-XRD), Powder X-ray diffraction (PXRD) and Scanning Electron Microscopy coupled with Energy Dispersive X-ray Spectroscopy (SEM-EDS) were employed to characterise the mineral phases and crystal structures and Ion Chromatography (IC) and Inductively Coupled Plasma-optical Emission Spectrometry (ICP-OES) were used to assess the chemical composition of the solution in the initial and final time segments of the experiments.

1.1. Theoretical framework

The Enzyme-Mediated Multiphase Precipitation (EMMP) method is driven by a precipitation solution containing crude urease extract, bone meal, and urea, which induces the formation of mineral phases. The immobilization of EMs through EMMP in aqueous solutions occurs through multiple pathways involving mineral precipitation, functional group binding, electrostatic/ion exchange interactions, and adsorption mechanisms that combined enhance the immobilization of toxic metal ions, reducing their mobility and bioavailability. These pathways do not act independently; they operate within a broader biogeochemical framework that integrates biocatalysis, geochemical transformations, and organic-mineral interactions. This integrated perspective, referred to as biogeochemical trapping, describes the collective set of biological, chemical, and geological interactions that may contribute to metal immobilization through biogeotechnical methods in aqueous environments (Gadd, 2010; Borch et al., 2010), providing an efficient pathway for metal immobilization beyond conventional physicochemical mechanisms that rely on a single immobilization route. Anthropogenic EMs contamination in water and soil is a major environmental issue in many urban areas. This increased concentration of EMs in soil and groundwater is not merely a significant public health matter but is also responsible for hindering ecosystem services such as nutrient cycling, soil fertility and carbon sequestration that are indispensable in a liveable city (IPCC, 2022). Sustainable land-use practices, pollution remediation and prevention, and conservation efforts that consider soil and groundwater are essential for maintaining the health and functionality of these vital ecosystems. Protecting soil and groundwater ecosystem services is necessary to guarantee water and food security, ecological health, and resilience to environmental change (UN, 2021).

Given the need for effective strategies to mitigate EMs contamination and restore ecosystem services, innovative biogeotechnical approaches have been explored for wastewater and soil remediation and stabilisation. Among these, Microbial Induced Carbonate Precipitation (MICP) and Enzyme Induced Carbonate Precipitation (EICP) have gained attention as sustainable techniques with the potential to immobilise EMs and simultaneously sequester carbon dioxide from the atmosphere or waste sources (Wilcox et al, 2025). MICP and EICP rely on urease enzymes produced by ureolytic microorganisms or directly extracted from plants or organisms to catalyse the hydrolysis of urea into ammonia and carbon dioxide, leading to the precipitation of calcium carbonate (CaCO3). The enzymatic and microbial processes that induce carbonate precipitation can also be leveraged to immobilise and sequester contaminants in wastewater and the soil matrix (Bian et al., 2024; Zeng et al., 2025). Both techniques proved to be efficient in immobilising inorganic contaminants predominantly through mechanisms of direct precipitation, co-precipitation, adsorption and surface complexation in distinct environmental contexts, such as groundwater and wastewater (Torres-Aravena et al., 2018; Zhong et al., 2022), soil improvement and erosion control (Hamdan & Kavazanjian, 2016; 2016; Almajed et al., 2020, 2021; Arab et al., 2021; Moghal et al, 2020; Bian et al., 2024) and mining waste (Makinda et al., 2023; Zhang & Zhang, 2024; Wilcox et al., 2024). However, the ureolytic precipitation of carbonates generates substantial amounts of ammonium, which transforms into ammonia through pH-dependent equilibrium and can lead to environmental issues such as eutrophication, bio-toxicity, soil acidification, and formation of inorganic secondary particulate matter (Behera et al., 2010; Park et al., 2021).

Several methods have been proposed for the remediation of ammonium, such as ion exchange, struvite ($(NH_4)MgPO_4 \cdot 6H_2O$) precipitation, nitrification/denitrification, and adsorption (Yuan et al., 2024; Gowthaman et al., 2022; Crane et al., 2022). Combining these methods can often yield the best results, leveraging the strengths of each method to effectively manage and remove ammonium byproducts from MICP and EICP processes applied in soil and water. A significant challenge lies in the fact that once released into the environment, ammonium tends to be chemically adsorbed in the clay minerals or organic matter of the soils; it can also be dispersed through water systems or be transformed into gas ammonia, depending on the pH of the media. Managing and mitigating the dispersion of ammonium [NH_4^+] and its transformation into ammonia [NH_3] in the environment requires a strategic approach that involves containment and treatment. Although proven effective for ammonium remediation, the cited methods - combined or individually - constitute independent secondary treatment strategies that introduce additional steps to the initial remediation process, increasing both process complexity and operational costs. Selecting the appropriate method, or combination of methods, depends on factors such as the scale of the project, local environmental conditions, and specific site requirements while evaluating their economic feasibility and environmental trade-offs through Life Cycle Assessment (LCA) can provide crucial insights into their long-term sustainability and cost-effectiveness.

In light of these challenges, alternative approaches that address soil remediation and ammonium management in a single process have emerged. Phosphate precipitation mediated by enzymes or microbial activity is a dynamic and potent method for remediating contaminated soils and water, particularly in environments polluted by heavy metals and radionuclides, with

demonstrably high remediation performance across a range of contaminants and environmental conditions (Lai et al., 2023; Han et al., 2022). The precipitation of phosphates induced by ureolytic processes has two important additional benefits when compared to EICP and MICP: 1) some of the precipitated phosphate phases like struvite and brushite can sequester the ammonium byproduct via mechanisms of precipitation and adsorption, and 2) due to general lower solubility, phosphates demonstrate better performance in stabilising heavy metals compared to carbonates, particularly for Pb and Zn, remaining immobilised in a broader range of pH, even in more acidic conditions (Jiang et al., 2020; Han et al., 2022; Yu et al., 2020).

In this study, we investigated the efficiency of Enzyme-Mediated Multiphase Precipitation (EMMP), a novel technique inspired by EICP and phosphate precipitation techniques that generate less ammonium byproduct than conventional EICP methods during EMs immobilisation. EMMP uses plant-derived urease crude extract, bone meal, and urea to precipitate carbonates, calcium phosphate compounds (CPCs) and metal-magnesium ammonium phosphates (M-struvite species) in just one stage.

We propose the use of local waste materials in a "waste-to-resource" approach and optimise the method based on life cycle assessment and greenhouse gas (GHG) protocol principles to decrease the consumption of non-renewable goods, GHG emissions and overall environmental impact and costs. This approach was employed to evaluate how EMMP's effectiveness in immobilising EMs and ammonium through immobilisation within the precipitated phases varies across nine specific metals – Cd, Co, Cu, Cr, As, Li, Ni, Pb and Zn. Additionally, by looking at the underlying mechanisms behind the variations in heavy metal immobilisation and residual levels of ammonium, we aim to demonstrate how incorporating waste-derived materials can maintain the same efficiency level as commercially available products while enhancing the sustainability of EMMP.

To assess the efficiency of EMMP in decreasing the concentration of EMs in water, we performed a series of test tube experiments with three different concentrations of EMs individually. Single Crystal X-ray diffraction (SC-XRD), Powder X-ray diffraction (PXRD) and Scanning Electron Microscopy coupled with Energy Dispersive X-ray Spectroscopy (SEM-EDS) were employed to characterise the mineral phases and crystal structures and Ion Chromatography (IC) and Inductively Coupled Plasma-optical Emission Spectrometry (ICP-OES) were used to assess the chemical composition of the solution in the initial and final time segments of the experiments.

1.1. Theoretical framework

The Enzyme-Mediated Multiphase Precipitation (EMMP) method is driven by a precipitation solution containing crude urease extract, bone meal, and urea, which induces the formation of mineral phases. The immobilization of EMs through EMMP in aqueous solutions occurs through multiple pathways involving mineral precipitation, functional group binding, electrostatic/ion exchange interactions, and adsorption mechanisms that combined enhance the immobilization of toxic metal ions, reducing their mobility and bioavailability. These pathways do not act independently; they operate within a broader biogeochemical framework that integrates biocatalysis, geochemical transformations, and organic-mineral interactions. This integrated

perspective, referred to as biogeochemical trapping, describes the collective set of biological, chemical, and geological interactions that may contribute to metal immobilization through biogeotechnical methods in aqueous environments (Gadd, 2010; Borch et al., 2010), providing an efficient pathway for metal immobilization beyond conventional physicochemical mechanisms that rely on a single immobilization route.

1.1.1. Mineral Precipitation

Mineral precipitation via EMMP primarily occurs through urease-driven biochemical reactions that facilitate carbonate and phosphate formation. The cementation solution provides the necessary enzymatic activity, biomolecules, and ions that drive the process. Factors such as pH, ionic composition, and the presence of organic and inorganic molecules further influence the stability, transformation, and evolution of the resulting mineral phases. In addition to enzyme-mediated processes, direct precipitation can also take place when metal ions react with available carbonate or phosphate species in solution, leading to the formation of insoluble mineral phases.

1.1.1.1. Urease-Driven Carbonate and Phosphate Precipitation

The core of EMMP mineral precipitation should begin with the urease-catalysed hydrolysis of urea (Lai et al., 2023):

$$CO(NH_2)_2 + H_2O \xrightarrow{urease} 2NH_3^+ + CO_3^{2-}$$

This reaction generates carbonate ions, which contribute to mineral formation while simultaneously increasing the system's pH due to ammonium production. At first, in acidic conditions (pH 3-4), most ammonia (NH_3) is protonated into ammonium (NH_4^+), but as the reaction progresses, NH_3 accumulates and reacts with water, producing hydroxide ions (OH^-) and gradually increasing ph.

$$NH_3+H_2O \leftrightarrow NH_4^+ + OH^-$$

As the pH continues to rise, the system transitions from acidic to alkaline conditions allows the participation of atmospheric CO_2 in the carbonate precipitation process through equilibrium reactions:

$$CO_2(g) \rightleftharpoons CO_2(aq) + H_2O \rightleftharpoons H_2CO_3 \rightleftharpoons HCO_3^- + H^+ \rightleftharpoons CO_3^{2-} + 2H^+$$
$$Ca^{2+} + CO_3^{2-} \rightarrow CaCO_3$$

Simultaneously, phosphate ions present in solution participate in multiple precipitation pathways forming calcium phosphate compounds (Gowthaman et al., 2023):

$$Ca^{2+} + PO_4^{3-} + OH^- \rightarrow Ca_{10}(PO_4)_6(OH)_2 \text{ (hydroxyapatite)}$$

$$Ca^{2+} + HPO_4^{2-} \rightarrow CaHPO_4 \text{ (brushite)}$$

Additionally, the presence of magnesium and ammonium enables the formation of struvite-family minerals:

$$Mg^{2+} + NH_4^{+} + PO_4^{3-} + 6H_2O \rightarrow MgNH_4PO_4 \bullet 6H_2O \text{ (struvite)}$$

1.1.1.2. Direct Bonemeal-Induced M Precipitation

Bone meal extract serves as a rich source of calcium (Ca^{2+}) and phosphate (PO_4^{3-}) ions, which facilitate hydroxyapatite ($Ca_{10}(PO_4)_6(OH)_2$) precipitation and other metal-phosphate mineral formations (Cao et al., 2003), depending on metal availability, pH conditions, and solution chemistry. Heavy metals such as Pb^{2+}, Cu^{2+}, and Zn^{2+} can either substitute for calcium within the hydroxyapatite structure or form separate phosphate precipitates (Ma et al., 1995; Xu et al., 1994). Phosphate-based minerals such as pyromorphite ($Pb_5(PO_4)_3Cl$), copper phosphate ($Cu_3(PO_4)_2$), and zinc phosphate ($Zn_3(PO_4)_2$) may also form, with amorphous calcium phosphate (ACP) serving as an intermediate phase (Li et al., 2021). This process is particularly effective for lead (Pb^{2+}), which preferentially forms pyromorphite ($Pb_5(PO_4)_3Cl$), a highly stable phase under a wide range of environmental conditions (Ryan et al., 2001; Li et al., 2021). Furthermore, competitive ions such as carbonate and sulphate can influence precipitation pathways and the phase stability of the resulting mineral products.

1.1.2. Functional group binding

EMs can also be immobilized by interacting with specific functional groups present in organic molecules derived from soybean and bone meal, including proteins, peptides, polysaccharides, and lipids. These interactions rely on chelation, complexation, and covalent bonding, which contribute to metal immobilization at a molecular level (Chirakkara et al., 2006; Liu et al., 2013). In addition to these biomolecules, bone meal contains collagen, phosphoproteins, and glycoproteins, which provide additional functional groups for metal binding, enhancing sequestration pathways.

Biomolecules containing sulfhydryl (-SH) groups exhibit a strong affinity for soft metal ions such as Pb^{2+}, Cd^{2+}, and Hg^{2+}, forming highly stable metal-thiolate complexes (Ajsuvakova et al., 2020).

Sulfur-containing amino acids in soybean proteins, particularly cysteine and methionine, are known to bind heavy metals through thiol-metal interactions, forming stable thiolate complexes (Liu et al., 2013). Although specific studies on soybean proteins are still emerging, the role of sulfur-containing functional groups in metal binding has been extensively reported for carbon-based adsorbents. Yang et al. (2019) demonstrated that the introduction of sulfur functional groups (e.g., thiol, sulfonic) onto activated carbon, graphene oxide, and carbon nanotubes significantly enhances their capacity to adsorb metals such as Pb(II), Cd(II), and Hg(II) through surface complexation and precipitation mechanisms. Bulgariu et al. (2021) did not investigate molecular-level mechanisms, but their study confirmed the high sorption capacity of

alkaline-treated soybean waste biomass for Pb^{2+}, Cd^{2+}, and Zn^{2+}, suggesting the presence of diverse functional groups that facilitate metal retention.

Carboxyl (-COOH) functional groups, commonly found in proteins, peptides, and organic acids, contribute to metal sequestration by forming stable coordination complexes with metal ions (Liu et al., 2013). This process is particularly relevant for Pb^{2+}, Zn^{2+}, Cu^{2+}, and Ni^{2+}, where carboxyl groups facilitate metal binding through ligand exchange, stabilizing metal-organic interactions and reducing solubility in solution.

Amino groups ($-NH_2$), abundant in peptides and proteins, also play a crucial role in metal coordination but through distinct mechanisms. These groups function as electron donors, forming coordination bonds that stabilize metal ions in solution and facilitate their retention in organic structures (Yang et al., 2019; Vandenbossche et al., 2015). This interaction is particularly relevant for Cu^{2+}, Ni^{2+}, and Zn^{2+}, as amine ligands can modulate metal speciation, influence redox behaviour, and contribute to the stabilization of metal-protein complexes.

The efficiency of metal binding varies depending on the specific biomolecular interactions. Studies indicate that proteinaceous components of crude urease extracts exhibit a preferential affinity in the order of Zn > Ni > Cr, likely due to differences in coordination chemistry and molecular conformation (Liu et al., 2013; Singh, 2017). Similarly, proteins and phosphoproteins from the bonemeal solution provide additional metal-binding sites, potentially altering selectivity patterns and influencing sequestration pathways. This suggests that biomolecular interactions not only aid in metal sequestration but may also affect the preferential incorporation of certain metals into mineral phases.

1.1.3. Electrostatic Attraction

Adsorption is another key pathway for metal immobilization in enzyme-mediated systems, involving both biomolecular surfaces (proteins, polysaccharides, phosphoproteins) and mineral phases ($CaCO_3$, hydroxyapatite, and other precipitates). Physisorption occurs through weak van der Waals forces and electrostatic attraction, leading to reversible metal attachment onto these surfaces, whereas chemisorption involves stronger covalent or ionic bonding with functional groups such as carboxyl (-COOH), amine ($-NH_2$), and sulfhydryl (-SH) (Liu et al., 2013). Moreover, chemisorption may involve charge transfer mechanisms, where metal ions share or transfer electrons with biomolecular ligands or mineral surfaces, forming stable coordination complexes.

Surface complexation further contributes to adsorption, as metal ions displace water molecules in their hydration shells and directly bond with functional groups via ligand exchange reactions (Huang et al., 2014). This mechanism is particularly relevant for divalent metal cations such as Zn^{2+}, Ni^{2+}, and Cu^{2+}, which exhibit a strong affinity for carboxyl and amine groups on biomolecules, as well as reactive sites on mineral surfaces (Gupta & Balomajumder, 2015).

The efficiency of adsorption depends on metal competition for binding sites, with sequestration capacity varying under different environmental conditions. Organic molecules, including proteins and polysaccharides in crude urease extracts, as well as phosphoproteins, collagen, and bone-derived glycoproteins from bonemeal, modify the surface charge and hydrophilicity of both biomolecules and mineral precipitates, affecting their adsorption affinity.

Studies suggest that metals with higher charge densities, such as Zn^{2+} and Ni^{2+}, tend to form more stable inner-sphere complexes, whereas larger, more electropositive ions exhibit weaker interactions (Singh, 2017).

1.1.4. Evolution of Mineral Phases

Organic molecules in crude urease extracts and bone meal play a crucial role in mineral nucleation and growth, acting as nucleation sites and influencing mineral morphology. Proteins and polysaccharides can stabilize amorphous or metastable phases before they transition into more thermodynamically stable minerals (Tange et al., 2021). Biomolecule-mediated interactions further influence mineralization by introducing functional groups (-COOH, -NH_2, -OH) that modify crystal formation and stabilization (Weiner & Addadi, 2011). These biomolecules can function as nucleation sites, guiding the precipitation of phosphates and carbonates into structurally stable phases (Takagi & Chow, 1998; Rivadeneyra et al., 2010).

Once precipitated, mineral phases undergo transformations due to thermodynamic and kinetic conditions. Some minerals crystallize directly into their stable forms, while others evolve through dissolution-reprecipitation, Ostwald ripening, or solid-state transitions (Gebauer et al., 2014). For example, calcium carbonate may initially precipitate as vaterite or aragonite before transforming into the more thermodynamically stable calcite phase (Zhu & Dittrich, 2016). Similarly, amorphous calcium phosphate (ACP) frequently serves as a precursor to hydroxyapatite, with its transformation influenced by pH, ionic strength, and biomolecular interactions (Pan et al., 2010).

Finally, carbonate and phosphate systems interact, leading to the formation of carbonate-substituted apatite or the conversion of calcite into phosphate phases in phosphate-rich conditions. This transition has been observed in biomineralization and hydrothermal studies, where calcium carbonate acts as a precursor for hydroxyapatite via dissolution-reprecipitation mechanisms (Dorozhkin, 2012).

2. Material and Methods

2.1. Materials

We investigated mineral precipitation using synthetic solutions individually spiked with one of nine EMs—As, Cd, Co, Cr, Cu, Li, Ni, Pb, and Zn—at three initial concentrations corresponding to treatment levels: T1 (2 mM), T2 (5 mM), and T3 (20 mM). The experimental setup included a crude urease extract derived from soybean (*Glycine max*), powdered urea added to the EM solution to achieve a final concentration of 1 M, and a bonemeal solution serving as a source of Ca, P, Mg, and K. Bonemeal (Westland) was obtained from a local garden centre, and soybeans (Jalpur) were purchased from a local supermarket.

Urea (98% purity) and the metal reagents—$CdCl_2$, $CoCl_2$, $Cr_2(SO_4)_3 \cdot xH_2O$, $CuCl_2$, $AsCl_3$, LiCl, $NiCl_2$, $PbCl_2$, and $ZnCl_2$—were purchased from Sigma-Aldrich. All metal salts were anhydrous, in powder form, and had a trace metals basis purity of ≥99.995%. Deionised water with a resistivity of 18.2 MΩ·cm, produced by the Milli-Q Ultrapure and Pure Water Purification

System in the Environmental Biogeochemistry laboratory at the University of Glasgow, was used to prepare all solutions.

2.1.1. Bone meal solution preparation

The bonemeal solution (BMS) was prepared with slight modifications to the method proposed by Gowthaman (2023). Specifically, 50 grams of bonemeal were added to a beaker containing 250 mL of deionized water and 60 mL of 1 M hydrochloric acid. The mixture was stirred for 2–3 minutes, left to rest overnight, and filtered the following day using Grade 2 laboratory filter paper. The composition of the resulting solution was analysed using ICP-OES (see below section 2.4 for full methods), with the concentrations of the primary components presented in Table 1. Additionally, the pH and electrical conductivity were measured using a YSI sensor and normalized to a standard temperature of 25°C.

Table 3
Electroconductivity (EC), pH and average (N = 7) concentration of Mg, Ca, K and P in the bonemeal solution.

Ca (ppm)	K (ppm)	Mg (ppm)	P (ppm)	pH	EC (uS/cm)
14577.00 ± 132.5	266.50 ± 6.37	316.50 ± 8.41	6349.00 ± 77.59	3.35 ± 0.31	167 ± 5.00

2.1.2. Preliminary Optimization of Soybean Concentration and Operational Parameters

The optimization of soybean concentration and operational parameters was evaluated through direct mass measurement of precipitates. Soybean extracts were prepared at concentrations of 20, 40, 60, 80, and 100 g/L in deionized water, each assessed with urea concentrations of 0.5, 0.75, and 1.0 M, while bone meal composition remained constant (Table 1). The experimental design encompassed both concentration variations and mixing ratio permutations, with each combination assessed in triplicate to ensure statistical validity. Quantitative analysis revealed that an 80 g/L soybean extract combined with 1.0 M urea solution and with bone meal solution in a ratio of 3:3:1, respectively, yielded the maximum precipitate mass under controlled laboratory conditions. Complete experimental protocols and raw data are provided in the Supplementary Materials.

2.1.3. Crude urease extract preparation

The crude urease extract (CUE) was prepared by combining 80 grams of soybeans with deionised water in a beaker until the total volume reached 1 L. The mixture was left overnight, then processed using a Fridja f1900 self-feeding cold press masticating juicer (1 L capacity, 250 W motor) to separate the solid and liquid components. The resulting liquid was mixed with calcium carbonate ($CaCO_3$) to achieve an approximate concentration of 0.06 M, facilitating the removal of excess protein. The mixture was left to decant for 2 hours, after which the supernatant was collected, centrifuged at 3700 rpm for 15 minutes at 4°C, and filtered using laboratory-grade

paper filter (Grade 2). Enzyme activity was measured using the method proposed by Whiffin (2004), yielding an activity of 2.44 mM urea·min^{-1}. A summary of the functions and proposed sources of the materials used in the EMMP mineralisation solution is provided in Table 2.

Table 2
Materials used in the EMMP mineralisation solution, their functions and proposed waste sources.

Material	Function	Waste Source of the Product
Soybean Crude Urease Extract (CUE)	Catalyser of urea hydrolysis	We propose using soybeans as a source of urease, given that they are the 5th most cultivated crop worldwide, with a significant global presence (FAO, 2024). Annually, copious quantities of soybeans are discarded due to quality control issues, presenting an opportunity for their utilisation as a urease source. Additionally, soy-based food industries could provide another viable source of soybean urease.
Urea	Substrate for urease; its hydrolysis catalysed by urease produces carbonate ions (CO_3^{2-}) and ammonium (NH_4^+).	Urea is a common waste in water treatment centres and can be sourced from animal and human urine.
Bonemeal solution (BMS)	Source of P, Mg and Ca	Bonemeal is a common food waste product derived from discarded fish and mammal carcasses.

2.2. Experimental procedure

To evaluate the immobilization of EMs using Enzyme-Mediated Mineral Precipitation (EMMP), a series of experiments were conducted using a cementation solution (CS). This solution was prepared by mixing urea, crude urease extract (CUE), and bone meal solution (BMS) in a 3:3:1 ratio, as determined by preliminary tests. CS was created by combining 110 mL of CUE, 110 mL of EMs solution in the desired concentration with added urea to achieve a 1M solution, and 36 mL of BMS. The mixture was then distributed into five 50 mL Falcon test tubes incubated at 25 °C for 72 hours until the end of the precipitation process, then left curing for 4 days. Afterwards, the precipitated content was washed with deionised water, filtered using Grade 2 filter paper, and placed in an oven at 37 °C for 24 hours. Aliquots of the residual liquid were collected for chemical composition analysis and for pH and electroconductivity measurements. The dried precipitates were stored in small plastic containers for characterisation.

2.3. Assessment of the immobilisation of EMs and ammonium production

The residual liquid generated during precipitation experiments was analysed to assess its efficiency in immobilising EMs and ammonium production. Residual liquid aliquots were first filtered using Grade 2 filter paper (Whatman) to remove solid matter. An aliquot of the residual liquid was filtered with 0.45 μm pore size syringe filters and used for colorimetric ammonium determination via the salicylate method using a SEAL AutoAnalyzer (AA3). To further evaluate pH and electrical conductivity (EC) measurements were conducted using a YSI ProDSS Multiparameter Probe. The measurements were recalibrated to 25 °C to ensure consistency in interpretation.

Nitric acid (HNO_3) was added to an aliquot of the filtered solution to achieve a final concentration of 2% (v/v). Subsequently, the solution was analysed using Inductively Coupled Plasma Optical Emission Spectroscopy (ICP-OES) (Thermo Scientific iCAP 7000), enabling the quantification of the final concentrations of the nine EMs. A full description of the analytical procedures used (including SEM, XRD, and ICP-OES) is provided in Supplementary Material section.

2.4. Characterization of the precipitates

For micromorphological studies, the precipitates formed during the experiments were separated into two fractions using a sieving system: one containing crystals larger than 1 mm and the other containing crystals smaller than 1 mm. The larger fraction was examined using a Zeiss stereomicroscope to observe their habit, colour, and size, providing a qualitative understanding of the macroscale features of the precipitates.

The smaller fraction, containing crystals below 1 mm, was analysed using scanning electron microscopy (SEM) to study their morphology and size in greater detail. Energy Dispersive X-ray Spectroscopy (EDS) was employed alongside SEM to verify the elemental composition of the precipitates and to correlate the observed morphologies with the two main mineral phases—calcite ($CaCO_3$) and struvite ($MgNH_4PO_4{\cdot}6H_2O$).

In addition, Powder X-ray Diffraction was performed using the entire precipitate powder, rather than a fraction, to identify the phases present and quantify the relative proportions of calcite and struvite for each element and treatment.

3. Results

3.1. System response parameters

This section presents four key system response parameters measured at the end of the curing period of the EMMP experiments. These parameters - pH, mass of precipitates, ammonium production, and metal removal efficiency - reflect the chemical and mineralogical responses of the system under the experimental conditions. The data have been divided into two figures to improve clarity and interpretability: Figure 1 presents pH and precipitate mass, while Figure 2 shows metal removal efficiency and ammonium production. Together, these figures illustrate distinct patterns for each metal across three treatments (T1–T3), corresponding to EMs concentrations of 2 mM (T1), 5 mM (T2), and 20 mM (T3) in the EMS solution. The control sample (without EMs) produced 12,877 ppm for ammonium production, compared to a theoretical maximum of 14,757 ppm, providing a baseline for comparing metal-specific responses.

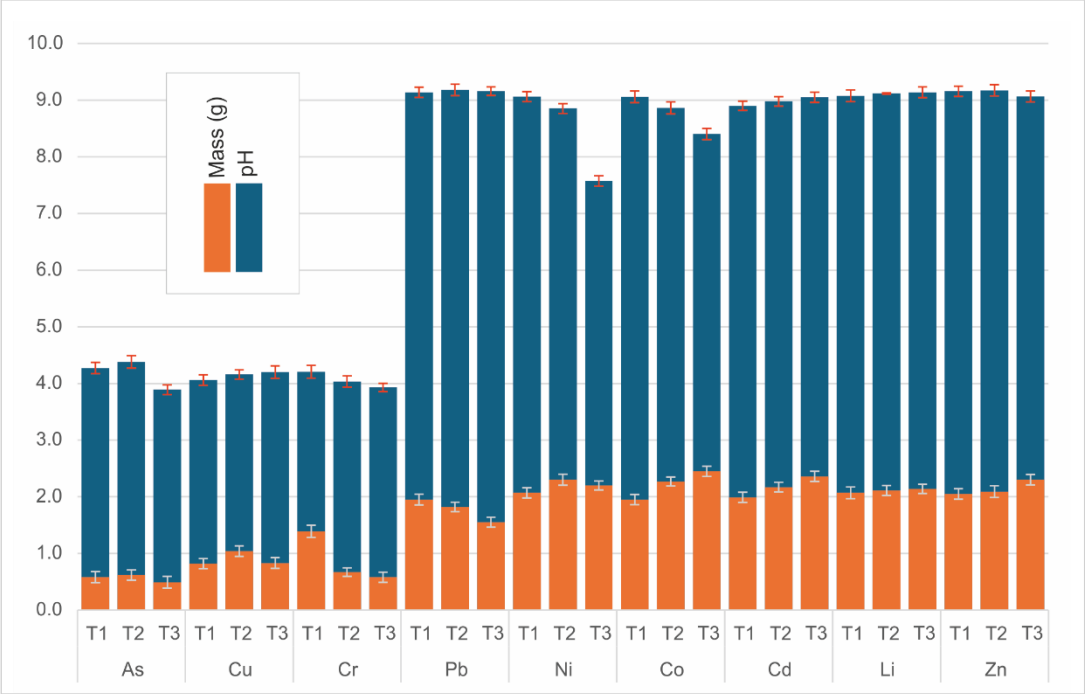

Figure 1. The figure presents pH levels (blue bars) and precipitate mass (orange bars) obtained at the end of the EMMP experiment across different elements and three treatments (T1, T2, T3). The left Y-axis corresponds to pH values, ranging from 1 to 10, while the right Y-axis corresponds to precipitate mass, measured in grams. Sample size is N = 5 for both metrics.

3.1.1. pH

The initial pH of the liquid ranged from 3.85 to 4.11 ± 0.1 for all metals. Based on their characteristic pH ranges in the residual liquid, the metals segregated into two distinct domains - an acidic domain (pH 4.2-4.8) and an alkaline domain (pH >7.5) (Figure 1).

In the acidic domain, arsenic showed a slight increase in pH from 4.07 in T1 to 4.18 in T2, followed by a significant drop to 3.89 in T3. Copper displayed a steady linear pH increase across treatments, from 4.08 in T1 to 4.20 in T3. Chromium experienced a consistent drop in pH, from 4.21 in T1 to 3.93 in T3.

In the alkaline group, consisting of Pb, Ni, Co, Cd, Li, and Zn, varied pH behaviours were observed. Lead maintained a highly stable alkaline pH across treatments, ranging from 9.14 in T1 to 9.16 in T3. Nickel exhibited a decreasing pH trend, from 9.06 in T1 to 7.57 in T3. Similarly, cobalt showed a steady pH decline, from 9.06 in T1 to 8.40 in T3. Cadmium, lithium, and zinc demonstrated minimal pH variations, maintaining consistent alkaline conditions. Cadmium ranged between 8.90 and 9.05, while lithium and zinc maintained a narrow range of 9.08–9.14 and 9.16–9.07, respectively.

3.1.2. Mass of precipitates

Precipitate mass values are reported in grams. Over the treatment period, four metals—cobalt, cadmium, zinc, and lithium—exhibited an overall increase in mass with rising metal concentration (Figure1). Cobalt increased from 1.95 g to 2.45 g, while cadmium rose from 1.99 g

to 2.36 g. Zinc and lithium showed more moderate gains, with zinc increasing from 2.05 g to 2.30 g and lithium from 2.07 g to 2.14 g.

In contrast, two metals, lead and chromium, experienced consistent declines as metal concentrations increased. Lead decreased from 1.95 g to 1.55 g, whereas chromium exhibited a more pronounced drop from 1.39 g to 0.58 g.

The remaining three metals—copper, nickel, and arsenic—peaked at T2 before declining in T3. Copper rose from 0.82 g to 1.04 g before decreasing to 0.83 g, while arsenic increased from 0.58 g to 0.62 g before falling to 0.49 g. Nickel reached its highest mass at 2.30 g in T2, then slightly decreased to 2.20 g in T3, still exceeding its initial 2.07 g.

3.1.3. Ammonium production

The values presented in Figure 2 represent the percentage of ammonium produced relative to the control, with 100% corresponding to the average ammonium concentration measured in control samples (12,877 ppm). According to observed values (Figure 2), ammonium production fell into three distinct ranges: 1.73–4.31% (low), 16.56–48.97% (medium), and 69.47–85.97% (high).

In the low range, arsenic, chromium, copper, and lead showed varying patterns. Arsenic peaked at 4.19% in T2, between values of 3.46% and 2.80% in T1 and T3. Chromium declined steadily from 2.33% to 1.73%, while copper maintained stable values between 2.25–2.33%. Lead showed the highest initial value in this range at 4.31%, before decreasing to 2.02% by T3.

In the medium range, nickel and cobalt showed parallel declines—nickel from 24.94% to 16.56%, and cobalt from 32.90% to 17.71%. In contrast, cadmium increased steadily from 39.16% to 48.97% across treatments.

In the high range, lithium and zinc maintained the highest concentrations throughout. Lithium increased from 79.63% to 85.97% in T2, before stabilising at 85.80%. Zinc showed a gradual decline from 80.42% to 69.47% across treatments.

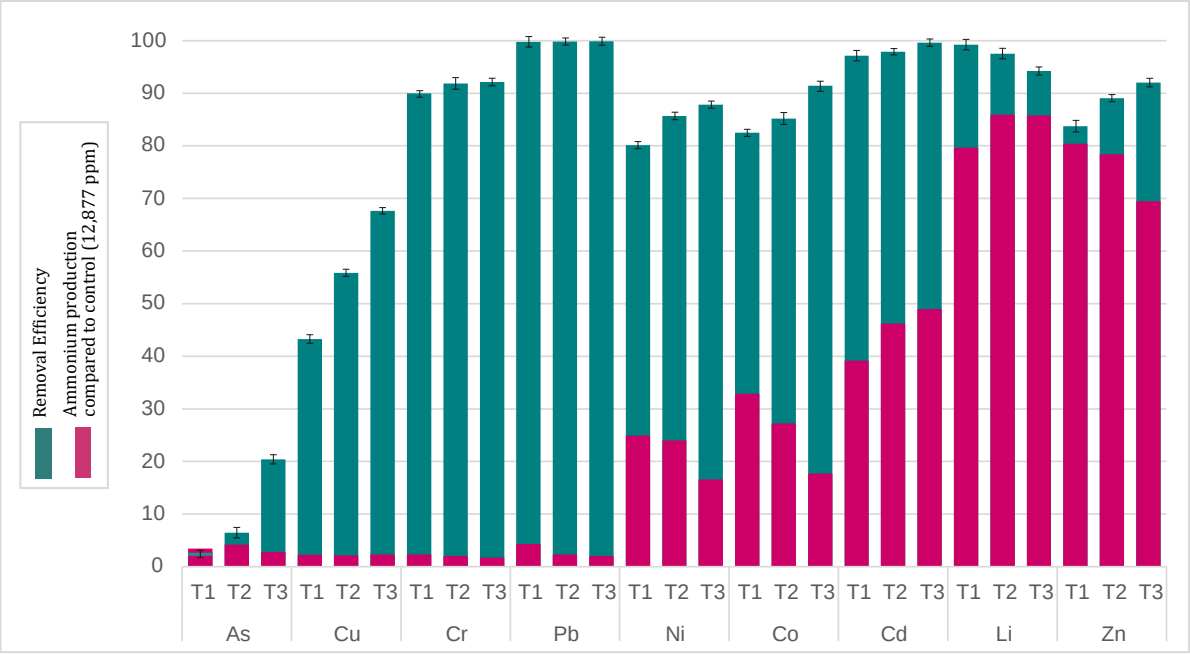

Figure 2. The figure presents removal efficiency (green bars) and ammonium production (purple bars) observed at the end of the EMMP experiment across different elements and three treatments (T1, T2, T3). The left Y-axis corresponds to removal efficiency, expressed as the average percentage of metal removal across five replicates (N = 5). The right Y-axis corresponds to ammonium production, expressed as a percentage relative to the maximum value obtained in the control sample (12,877 ppm).

3.1.4. EMs removal efficiency

As observed in Figure 2, three groups can be identified based on removal efficiencies: low (2.82–20.39%), medium (43.25–67.66%), and high (80.16–99.88%). Removal efficiency trends were analysed based on increasing metal concentration from T1 to T3.

In the low range, arsenic was the sole metal, with removal efficiency increasing from 2.82% to 20.39% as metal concentration rose. In the medium range, copper exhibited a steady improvement, increasing from 43.25% to 67.66% across treatments. The high removal efficiency range included the other seven metals. Lead exhibited the highest consistent removal rates, with an exceedingly small variation from 99.78% to 99.88%. In contrast, lithium experienced a slight decline, decreasing from 99.23% to 94.22%. The remaining metals in this category demonstrated progressive increases in removal efficiency: cadmium from 97.14% to 99.62%, chromium from 89.96% to 92.15%, nickel from 80.16% to 87.85%, cobalt from 82.48% to 91.44%, and zinc from 83.76% to 92.04%.

3.2. Micromorphological analysis of precipitates

3.2.1. Fraction > 1mm

Microscopic analysis of the precipitates, with the aid of natural light microscopy for the larger fraction (>1 mm) (Figure 3) and scanning electron microscopy (SEM) for the smaller fraction (<1 mm) (Figures 4 and 5), revealed notable consistency in their features across different

scales. Both imaging techniques confirmed the presence of two main mineral phases for all elements, except arsenic and copper, that produced mostly fine powder aggregates with little production of diminute crystals of calcite (arsenic in T2 and copper in T1 and T2).

The first phase, predominantly calcitic, consisted of crystals exhibiting a variety of morphologies, including spherical, star-shaped, botryoidal, and other structural variations (Figure 3B, F, G, H, I and 5A to I). The second phase, phosphatic, was dominated by coffin-like and needle-like struvite crystals (Figure 3B, C, D, E and 5J to N). Within both fractions, these well-defined crystals were embedded in a fine powder aggregate (FPA) (<10 µm), primarily composed of calcite, which can be observed in the background of images in Fig. 3A and 5A to N and the detailed morphology in Fig. 5 O to R.

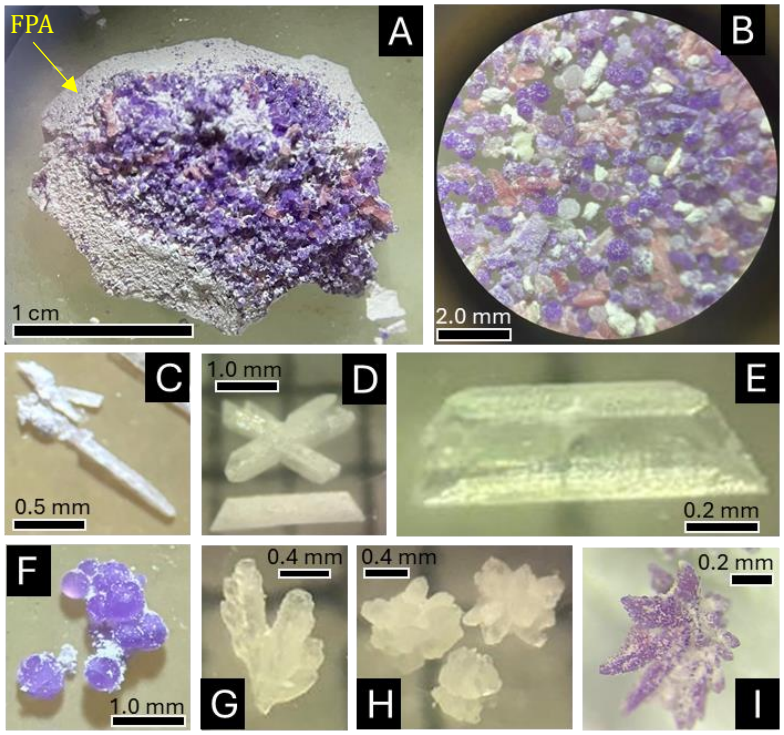

Figure 3. A) Co precipitate (T3) after oven drying step exhibiting larger crystals of calcite and struvite surrounded by a mass of very fine powder aggregate (FPA); B) Fraction of larger crystals under the microscope - natural light (Co-T3); C) Needle like crystal of calcite (Ni- T2); D) Butterfly and coffin-like struvite (Ni-T2); E) Coffin-like transparent struvite (Ni-T3); F) Spherical crystals are surrounded by a fine, loose calcitic powder (Co-T2); G, H) Star-like calcite (Cd-T2) and I) Star-like calcite (Co-T2).

3.2.2. Fraction < 1 mm

In this fraction the majority of treatments formed larger crystals of submillimetric calcite and struvite, consistently surrounded by a fine powder (< 5–10 µm) composed predominantly of calcite (Figures 4-A to H and 5 A to R). Table 3 presents the sizes and predominant morphologies of calcite and struvite crystals across all treatments for all elements, as observed through scanning electron microscopy (SEM), highlighting the variability.

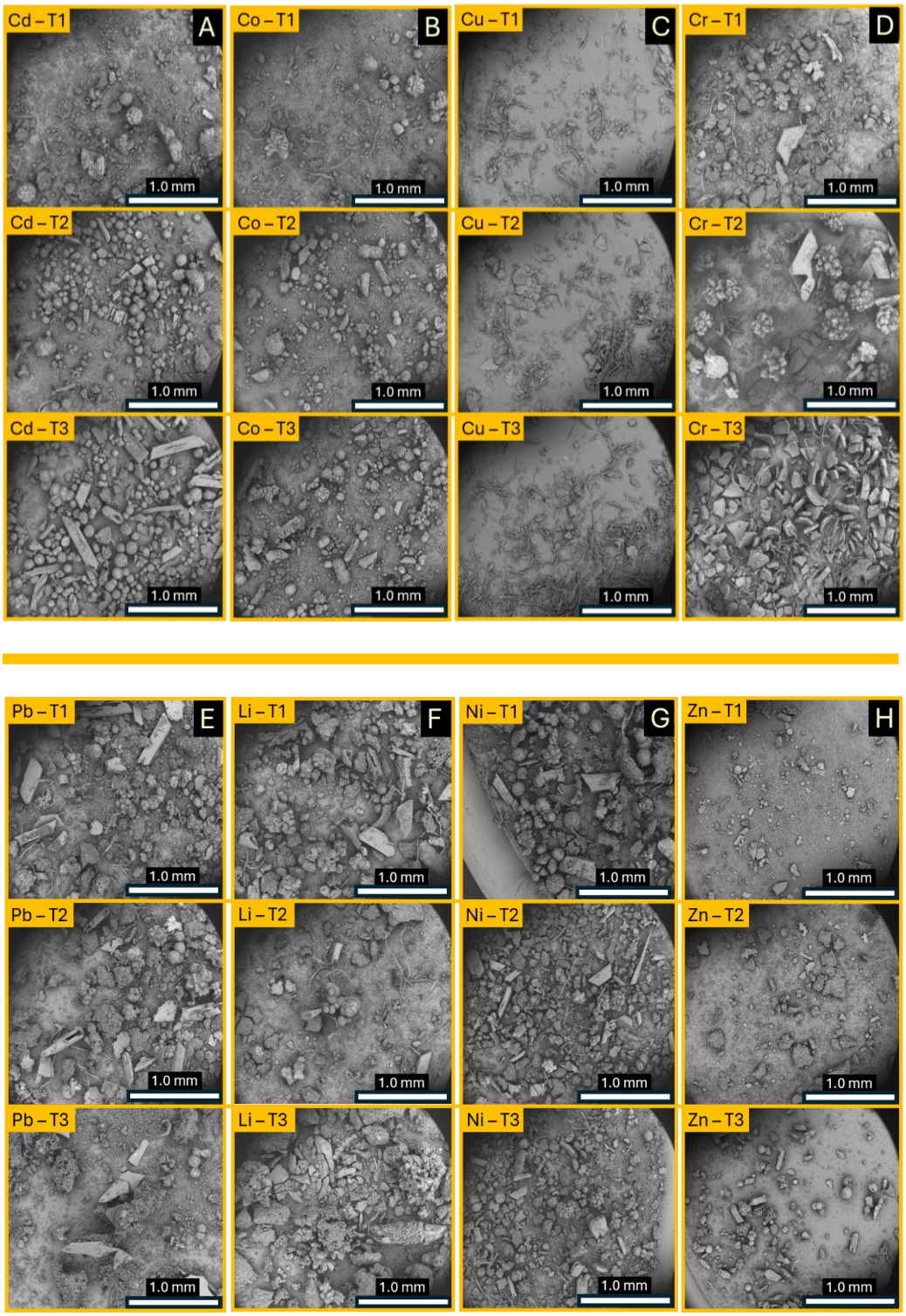

Figure 4. SEM backscattered images of a representative sample of precipitates formed in the presence of eight different metals under three treatments (T1, T2, T3). We used backscattered electron imaging as they enhanced resolution and contrast, allowing better differentiation of the morphological characteristics of the precipitates. Each column represents a metal (A: Cd, B: Co, C: Cu, D: Cr, E: Pb, F: Li, G: Ni, H; Zn), while each row corresponds to a treatment (top = T1, middle= T2 and bottom = T3). Arsenic was excluded as it did not yield enough material for analysis.

3.2.2.1.Micromoprphology of calcite, struvite, and fine crystals aggregates

Arsenic was excluded from analysis due to insufficient mass, though a few spherical crystals (0.05–0.1 mm) resembling calcite were observed in T2. Copper primarily formed fine powder aggregates (Fig. 4C), with only a few sparse, small fibrous radial calcite crystals (0.05–0.1 mm) in T1 and T2. Chromium produced calcite (0.20–0.65 mm) in T1 and T2, predominantly globular and star-shaped, whereas T3 resulted solely in fine aggregate material (Fig. 4D).

Across Li, Cd, and Co treatments (Fig. 4 A, B and F), calcite crystal size progressively decreased from T1 to T3. Lithium exhibited the broadest size range of crystals (0.10–0.65 mm), displaying spherical, globular, star-shaped, botryoidal, rare flower-like, and bone-like morphologies, with fibrous forms appearing in T3. Cadmium formed crystals (0.10–0.50 mm) with spherical, globular, star-shaped, and dumbbell-like habits, showing the greatest morphological diversity in T1. Cobalt produced calcite crystals (0.01–0.40 mm), with spherical, globular, and star-shaped morphologies, while both crystal size and diversity declined from T1 to T3. Across Li, Cd, and Co treatments, calcite crystal size progressively decreased from T1 to T3.

In Ni, Pb, and Zn treatments (Fig. 4 E, G and H), calcite crystal size exhibited a maximum in T2 before decreasing in T3. Nickel formed predominantly spherical, globular, and star-shaped crystals (0.10–0.30 mm), with simpler morphologies in T3. Lead generated large crystals (0.10–0.60 mm), exhibiting predominantly spherical, globular, and star-shaped morphologies. Zinc consistently formed small calcite crystals (0.05–0.30 mm), primarily spherical and globular, with the smallest crystals observed in T3. In Ni, Pb, and Zn treatments, calcite crystal size exhibited a maximum in T2 before decreasing in T3.

Across all treatments, hollow coffin-like was the dominant struvite morphology (Fig. 5M). Arsenic and copper treatments did not form struvite crystals, while chromium generated coffin-like struvite (0.10–0.75 mm) in T1 and T2, but T3 contained only fine aggregates (Fig. 5L).

Cadmium formed both coffin-like and prismatic crystals (0.20–0.90 mm) and cobalt exhibited coffin-like crystals (0.05–0.40 mm), and for both elements the crystals size decreased from T1 to T3. Lithium produced coffin-like and prismatic struvite (0.10–0.45 mm), whereas nickel displayed diverse habits, including twinned, needle-like, and plate-shaped crystals (0.10–0.95 mm, Fig. 5K, N), peaking in size at T2. Lead formed the larger coffin-like struvite crystals (0.05–1.0 mm). Zinc consistently produced smaller struvite crystals (0.05–0.20 mm). Li, Pb and Zn struvite crystals decreased in size from T1 to T3.

The fine powder aggregate appears in all treatments as a fine powder to the naked eye and is predominantly characterised by spherical to coral-shaped morphologies, which are indicative of calcite as the principal mineral phase in this fraction (Fig 5 O-P). Fig. 5 Q–R displays submillimetre-scale plaques composed of aggregates of ultrafine particles, which are likely to include poorly crystalline and amorphous phases that can be found in lead T3, chromium T3, and lithium T3 samples, as well as across all copper treatments.

Table 3

Size and morphologies of calcite and struvite in the smaller fraction of the precipitates (< 1 mm). T = treatment, calcite morphologies = Sp (Spherical), G (Globular), St (Star-like), D (Dumbbell), F (Flower-like), Fr (Fibrous-radial), B (bone-like and struvite), C (Coffin-like), P (Prismatic) and N (Needle-like). N/A indicates no crystal was formed, only aggregated powder. The measured crystal sizes may vary across images due to natural heterogeneity in the powder samples, as individual selections from such materials rarely exhibit uniform dimensions.

		Calcite								Struvite			
Element	T	Morphologies							Size (mm)	Morphologies			Size (mm)
		Sp	G	St	D	F	Fr	B		C	P	N	
Cadmium	1	●	●	●	●				0.10-0.50	●	●		0.20-0.50
	2	●	●	●	●				0.10-0.40	●	●		0.20-0.50
	3	●	●			●			0.10-0.25	●	●		0.30-0.90
Cobalt	1	●	●	●				●	0.10-0.40	●			0.05-0.10
	2	●	●	●	●				0.10-0.30	●	●		0.10-0.25
	3	●	●	●					0.10-0.20	●			0.10-0.40
Chromium	1	●	●	●				●	0.20-0.40	●			0.10-0.60
	2	●	●						0.30-0.65	●			0.10-0.75
	3	-	-	-	-	-	-	-	N.A.	-	-	-	N/A
Lead	1	●	●	●					0.10-0.50	●			0.20-1.00
	2	●	●	●					0.20-0.60	●			0.20-0.70
	3	●	●	●					0.05-0.30	●			0.05-0.20
Lithium	1	●	●	●		●			0.10-0.65	●			0.10-0.45
	2	●	●						0.10-0.30	●	●		0.10-0.30
	3	●	●	●		●	●		0.10-0.15	●	●		0.10-0.20
Nickel	1	●	●	●	●		●		0.10-0.20	●			0.15-0.80
	2	●	●		●		●		0.10-0.30	●	●	●	0.20-0.95
	3	●	●	●					0.10-0.20	●			0.10-0.60
Zinc	1	●	●						0.10-0.20	●	●		0.05-0.20
	2	●	●						0.10-0.30	●			0.05-0.20
	3	●	●						0.05-0.20	●	●		0.10-0.20
Copper	1						●		0.05-0.10	-	-	-	N.A.
	2						●		0.05-0.10	-	-	-	N.A.
	3	-	-	-	-	-	-	-	N.A.	-	-	-	N.A.
Arsenic	1	-	-	-	-	-	-	-	N.A.	-	-	-	N.A.
	2	●							0.10-0.20	-	-	-	N.A.
	3	-	-	-	-	-	-	-	N.A.	-	-	-	N.A.

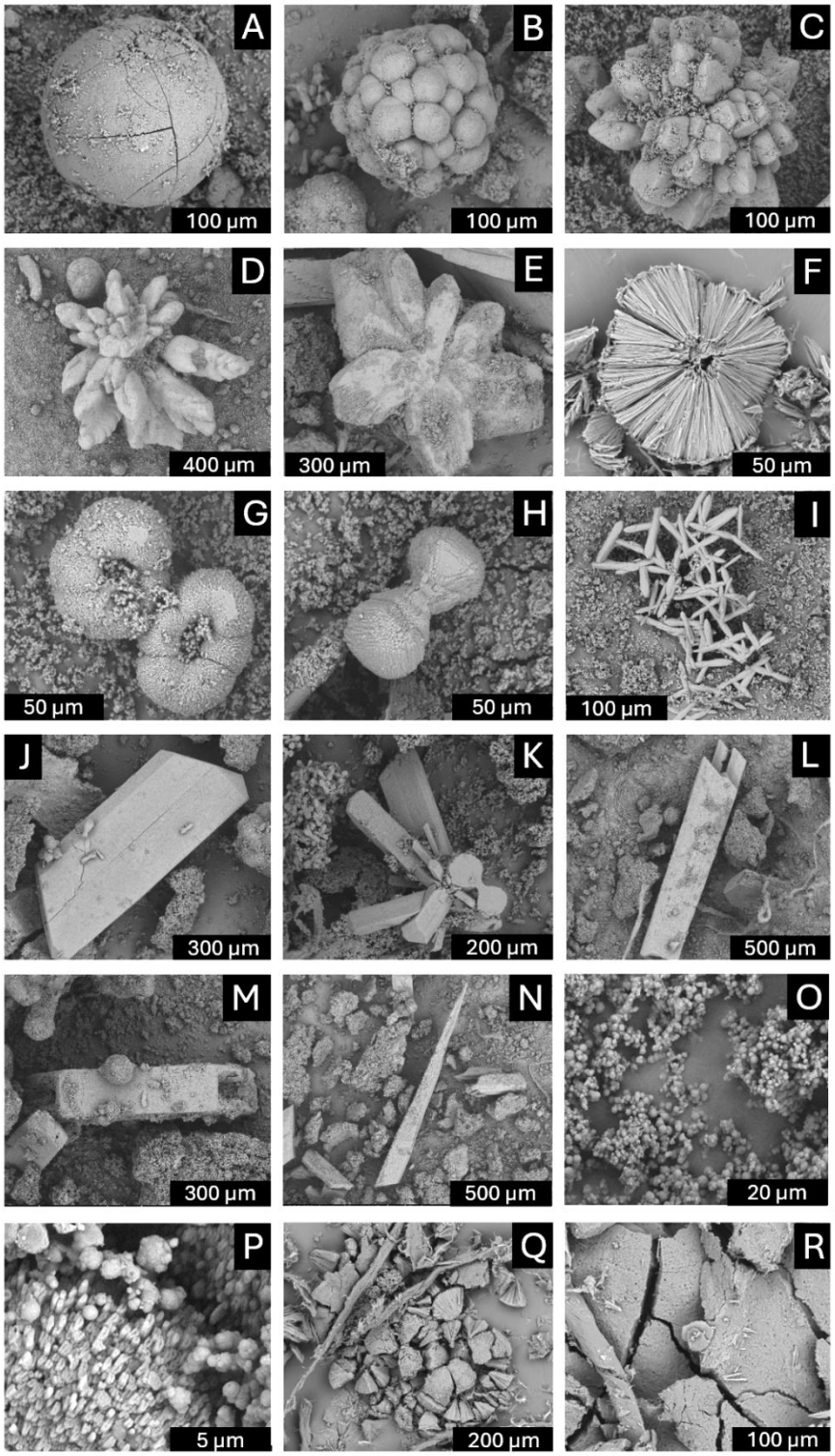

Figure 5. SEM micrographs of the predominant morphological variation of calcite and struvite crystals observed across various elements and treatment levels. Backscattered electron imaging was used to enhance resolution and contrast. (A) Spherical calcite (Cd-T1); (B) Botryoidal calcite (Li-T1); (C,D) Star-shaped calcite (Co-T1 and T2); (E) Flower-shaped calcite (Li-T1); (F) Fibrous-radial calcite (Cu-T1); (G) Donut-shaped calcite (Co-T2); (H) Dumbbell calcite (Cd-T1); (I) Bone-like calcite (Li-T1); (J) Coffin-shaped struvite (Ni-T1); (K) Twinned struvite (Ni-T1); (L) Prismatic struvite (Cr-T1); (M) Detail of hollow struvite (Pb-T1); (N) Needle struvite (Ni-T1); (O) Morphology of fine powder aggregates (Co-T3); (P) Detail of fine powder aggregates showing coral-like microstructure (Co-T2); (Q) Mass aggregates in Cr-T3; (R) Detail of mass aggregate (Cr-T3).

3.3. Powder XRD

The diffractograms (Figure 6) show the precipitation patterns, indicating variations in the relative proportions of the two main crystalline phases, calcite and struvite, across treatments for each element. Minerals from the apatite group were also identified in some treatments through XRD Rietveld refinement. Although distinct apatite peaks were not visually discernible in the raw diffractograms, likely due to low abundance, peak overlap, and poor crystallinity, Rietveld refinement confirmed the presence of chlorapatite and hydroxyapatite, with contents ranging from 0.95% to 5.1%, depending on the EMs and treatment. Crystals of apatite were not observed in either the larger or smaller fractions, suggesting that this phase is confined to the fine powder aggregate fraction. Arsenic and copper were excluded from the analysis due to insufficient mass for characterisation. Table 4 presents the relative percentages of the crystalline phases, calculated using Profex software version 5.4.1. (Döbelin et al., 2015). These percentages are expressed as relative values, as no internal standard was employed to allow absolute quantification.

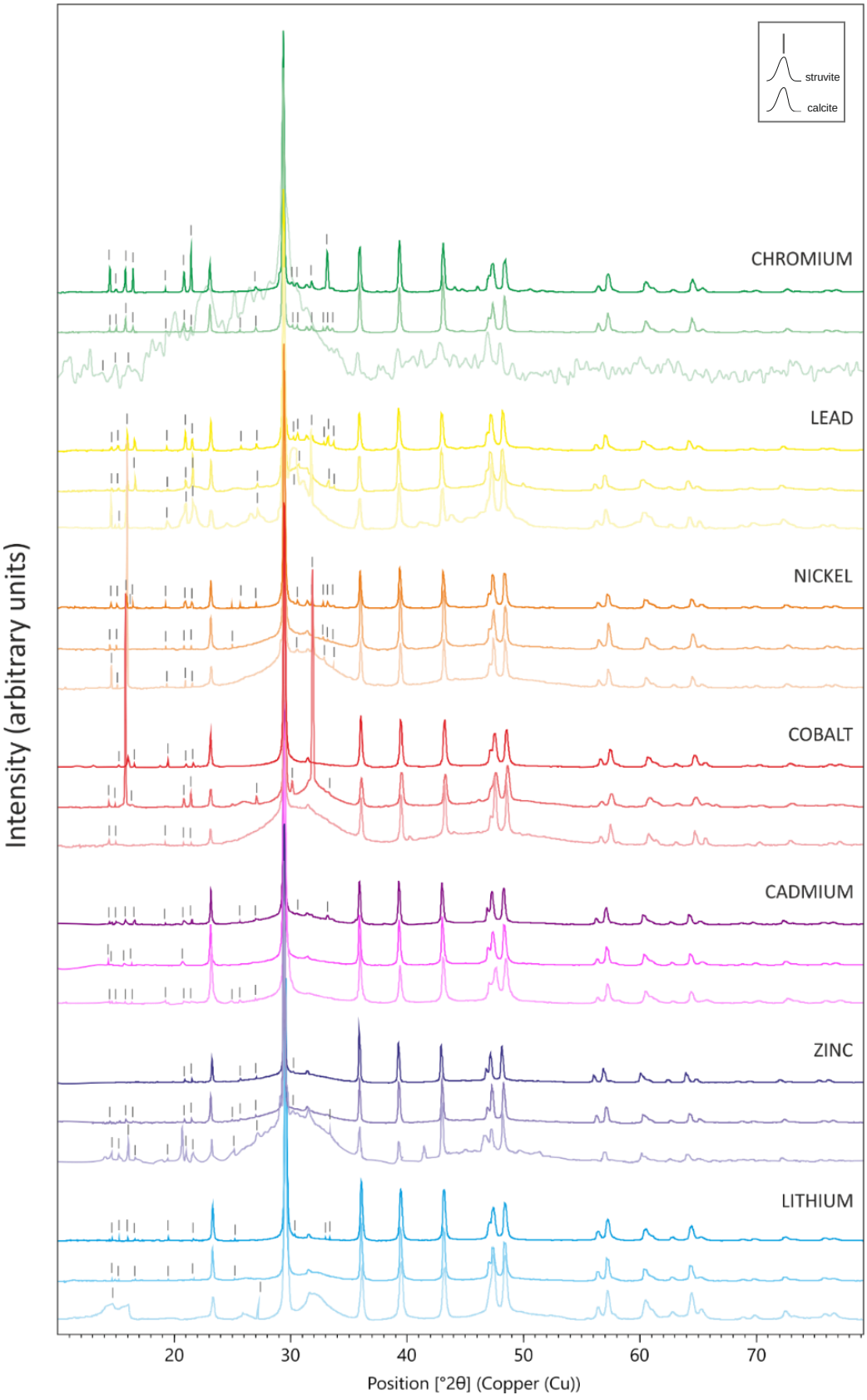

Figure 6. Stacked XRD diffractograms illustrating the crystallization of calcite and struvite in the presence of cobalt, nickel, lead, chromium, lithium, zinc, and cadmium across three treatment levels (T1- top line, T2 - middle line, T3 - bottom line). The marked peaks correspond to struvite and the non-marked to calcite.

Table 4

Percentage of major (calcite and struvite) and accessory phases (apatite group) identified in the precipitates. Phase proportions were determined using Profex software based on relative abundances, without the application of an internal standard. T = Treatment; N.A. Non applicable. Trace (-) phase not identified.

		Main Phases		Minor and Accessory Phases			TOTAL (%)
Element	T	Calcite (%)	Struvite (%)	Chlor apatite (%)	Hydroxy apatite (%)	Apatite (%)	
Cadmium	1	87.15	9.32	-	4.37	-	99.84
	2	87.78	11.78	-	1.27	-	100.85
	3	96.36	3.78	-	-	-	100.14
Cobalt	1	91.66	6.03	2.44	-	-	100.13
	2	81.90	17.19	0.95	-	-	100.04
	3	91.47	8.61	-	-	-	100.08
Chromium	1	76.70	20.52	-	-	2.86	100.08
	2	89.84	9.07	-	-	1.25	100.16
	3	N.A.	N.A.	N.A.	N.A.	N.A.	N.A.
Lead	1	86.43	8.58	5.11	-	-	100.11
	2	82.84	12.87	4.40	-	-	100.11
	3	85.67	11.42	3.76	-	-	100.79
Lithium	1	87.04	8.81	3.11	-	-	99.95
	2	90.61	6.41	2.67	-	-	99.82
	3	N.A.	N.A.	N.A.	N.A.	N.A.	N.A.
Nickel	1	85.75	10.37	4.31	-	-	100.43
	2	92.24	5.85	2.04	-	-	100.13
	3	81.47	17.63	1.76	-	-	100.86
Zinc	1	95.42	4.60	-	-	-	100.02
	2	93.11	6.97	-	-	-	100.08
	3	90.88	9.24	-	-	-	100.12
Copper	1	N.A.	N.A.	N.A.	N.A.	N.A.	N.A.
	2	N.A.	N.A.	N.A.	N.A.	N.A.	N.A.
	3	N.A.	N.A.	N.A.	N.A.	N.A.	N.A.
Arsenic	1	N.A.	N.A.	N.A.	N.A.	N.A.	N.A.
	2	N.A.	N.A.	N.A.	N.A.	N.A.	N.A.
	3	N.A.	N.A.	N.A.	N.A.	N.A.	N.A.

The XRD diffractograms illustrate the evolving crystallisation behaviour of the two main phases in the system influenced by varying treatment levels across different elements. Chromium and lithium did not show enough crystallinity in T3 for a precise calculation of main phase percentages. For nickel, lead, chromium, lithium, and cadmium, sharper and more intense peaks are observed at T1, which progressively diminish toward T3. This trend suggests a higher degree of crystallinity at treatment levels with lower concentration of EMs. Interestingly, cobalt and zinc deviate from this pattern, displaying more intense and sharper peaks at T2 compared to T1, indicating that intermediate treatment levels create conditions more favourable for crystallisation, which then decline at T3. Arsenic and copper did not yield sufficient precipitate for XRD analysis.

The relative proportions of calcite and struvite varied across elements and treatments, with calcite consistently dominating the precipitates. Cobalt and lead displayed similar trends, with calcite reaching its highest proportions in T1 (91.66% and 86.43%, respectively), decreasing at T2 (81.9% and 82.84%), and increasing again at T3 (91.4% and 85.67%). Struvite showed an inverse pattern, peaking in T2 for both elements (17.19% for cobalt and 12.87% for lead) and decreasing at T1 and T3.

Cadmium and nickel also exhibited high calcite content across all treatments. Calcite content for cadmium was lowest at T2 (87.15%) and peaked at T3 (96.3%), while nickel displayed the highest calcite proportion at T2 (92.24%) and the lowest at T3 (81.47%). Struvite proportions followed complementary trends for these elements, with cadmium reaching its highest struvite content at T2 (11.78%) and nickel at T3 (17.63%).

Chromium, lithium, and zinc showed calcite as the predominant phase, with varying degrees of struvite content. Chromium exhibited calcite proportions of 76.7% at T1 and 89.8% at T2, while struvite decreased from 20.52% to 9.07%; no data were available for T3 due to insufficient precipitate mass. Lithium treatments showed calcite proportions of 87.04% at T1 and 90.61% at T2, with struvite proportions at 8.81% and 6.41%, respectively. Zinc showed decreasing calcite content from T1 to T3 (95.42% to 90.88%), while struvite proportions increased steadily, peaking at 9.24% in T3. Data for copper is unavailable due to insufficient precipitate mass for characterisation.

In addition to calcite and struvite, minerals from the apatite group were identified in cadmium, lead, lithium, and nickel treatments. The highest proportions were found in lead (5.11% in T1 and 4.40% in T2), followed by nickel (4.31% in T1 and 2.04% in T2), lithium (3.11% in T1 and 2.67% in T2), cadmium (4.37% in T1 and 1.27% in T2) and cobalt (2.44% in T1 and 0.95% in T2). No apatite-group phases were detected in treatments with arsenic, copper, chromium, or zinc. Notably, apatite phases were not observed in either the larger or smaller crystal fractions, suggesting they are confined to the fine powder aggregate.

4. Discussion

Our investigation into mineral precipitation mechanisms in EMMP applications reveals a complex interplay between enzymatic and non-enzymatic processes. While biogeotechnical methods such as EICP have traditionally attributed mineralisation and metal immobilisation solely to the urease activity of crude urease extracts (Almajed et al., 2020), our findings indicate a broader network of interacting mechanisms.

Although ureolysis-driven carbonate generation remains a principal driver of metal-carbonate precipitation in our experiments, primarily governed by pH-dependent equilibrium conditions (Ahenkorah et al., 2021), precipitation efficiency is influenced by multiple interdependent pathways, as outlined in Section 1.1. Furthermore, the temporal progression of crystallogenetic processes introduces an additional layer of complexity to the overall mineralisation dynamics.

A particularly noteworthy observation is the persistence of urease activity at pH values around 5.0—conditions traditionally considered suboptimal for urea hydrolysis. Although enzymatic activity increases with rising pH in most treatments, the detection of residual activity

below the generally accepted optimum range (pH 5–9) (Stocks-Fischer, 1999; Shu et al., 2022) suggests that the crude soybean extract retains partial catalytic functionality under mildly acidic conditions. This residual activity may arise from the inherent structural properties of soybean-derived urease, the presence of protective biomolecules in the crude extract or bone meal solution, or the formation of localised alkaline microenvironments (Krajewska, 2019). Previous studies have shown that proteins, polysaccharides, and phosphoproteins can enhance enzymatic resilience by forming hydration shells or shielding catalytic sites from pH-induced denaturation (Beaufils et al., 2021). Additionally, enzyme–mineral interactions may buffer local pH fluctuations, thereby stabilising catalytic performance in heterogeneous systems.

Of particular interest is the observation that immobilisation efficiency for elements such as As, Cu, Ni, Cr, and Pb increased across treatments despite a concurrent decline in precipitate mass. This decoupling between total mineral yield and immobilisation suggests that additional mechanisms of biosorption play a critical role at elevated metal concentrations. Bulgariu and Bulgariu (2018) demonstrated that the biosorption capacity of soy waste biomass increases with the initial concentration of metal ions, primarily due to enhanced concentration gradients that promote the diffusion of metal species towards active binding sites. Within EMMP systems, this may involve complexation with functional groups in soybean- and bone-derived biomolecules or sorption onto the surfaces of nascent mineral phases. Moreover, greater incorporation of metal ions into mineral structures via ionic substitution, chemisorption, or surface complexation may enhance immobilisation without proportionally increasing precipitate volume. These findings support a conceptual model wherein EMMP efficiency results from a combination of precipitation-based and sorption-driven processes, both of which become increasingly significant under metal-rich conditions.

To further explore element-specific behaviours in EMMP, the ecotoxic metals studied were classified based on their effects on urease activity and mineral precipitation dynamics. Some acted as high-impact inhibitors, markedly suppressing both urease activity and mineral formation under acidic conditions. Others functioned as low-impact inhibitors or even activators, with effects most pronounced in alkaline conditions, where they mildly suppressed or enhanced precipitation outcomes.

4.1. High-impact inhibitors (acidic domain)

Arsenic, copper, and chromium strongly inhibited urease activity, leading to lower pH, suppressed ammonium production, and reduced precipitate mass. Despite this, removal efficiency increased across treatments, albeit at different rates for each metal, indicating the existence of alternative sequestration pathways. Under acidic conditions, carbonate mineralisation was limited, and metal retention was instead likely governed by biomolecular interactions, adsorption, and direct phosphate precipitation or formation of amorphous or hydroxide-rich phases. These findings highlight the significance of non-carbonate immobilisation pathways in systems where urease-driven alkalisation is restricted.

4.1.1. Arsenic

Arsenic removal efficiency increased nearly tenfold from T1 to T3, despite a decline in pH, ammonium production, precipitate mass, and the limited formation of crystalline precipitates, suggesting that its immobilization was primarily driven by interactions with biomolecules combined with adsorption mechanisms.

At the lowest tested concentration (2 mM), urease retained partial activity, resulting in limited mineral precipitation. As concentration increased to 5 mM, there was a slight rise in precipitate mass, with sparse calcite crystals forming. At 20 mM, precipitate mass decreased further, indicating stronger inhibition of ureolysis and mineral precipitation. This inhibitory effect is likely attributable to arsenic binding to sulfhydryl groups in the urease active site and/or disruption of nucleation processes essential for crystal formation (Magomya & Barminas, 2017).

Arsenic exhibits low affinity for well-crystallised mineral phases such as calcite, where adsorption and structural incorporation are typically limited under experimental conditions, favouring the formation of amorphous phases over crystalline structures at high concentrations (Renard et al., 2015; Tardif et al., 2019). Nonetheless, recent studies have demonstrated that magnesium incorporation into the calcite lattice significantly enhances arsenic uptake by inducing lattice distortion, increasing surface charge density, and facilitating both the substitution of carbonate and hydroxyl groups and the formation of hydrogen bonds with As(III) (Gong et al., 2022). In addition, arsenic can also bind to proteins, interfering with processes necessary for mineral nucleation, though this may contribute to enhanced removal efficiency under certain conditions (Kumari et al., 2005).

In enzyme-mediated systems where both calcium and phosphate are available, arsenic immobilisation may occur through its incorporation into calcium phosphate phases. This mechanism has been demonstrated in biogeotechnical applications such as EICPP, where phosphate-rich waste sources induce the precipitation of calcium phosphate minerals under enzymatic control (Avramenko et al., 2024). Arsenate behaves similarly to phosphate and can substitute into apatite-like structures following the transformation $Ca_5(PO_4)_3OH \rightarrow Ca_5(AsO_4)_3OH$, reducing arsenic mobility (Lee et al., 2009). In environments with sufficient calcium and phosphate availability, arsenic may also form calcium arsenate ($Ca_3(AsO_4)_2$), a sparingly soluble compound that contributes to long-term sequestration (Yan et al., 2023). These precipitation pathways were likely supported by the bone meal solution, which provided a source of phosphate and calcium, facilitating arsenic entrapment in stable mineral phases. However, the efficiency of these reactions depends on system conditions, as arsenic-phosphate interactions can be influenced by competing sorption dynamics.

Studies have shown that arsenic can form stable complexes with functional groups such as carboxyl, hydroxyl, and amine groups in aqueous environments, promoting sorption onto biopolymers and mineral surfaces (Arai & Sparks, 2002). Under conditions where precipitation was inhibited, this process, facilitated by biomolecules from soybean extracts and bone meal, may have enhanced arsenic complexation and stability, ensuring its immobilization through non-mineral pathways (Manning & Goldberg, 1997; Czerniczyniec et al, 2007). Arsenic removal may have partially occurred through adsorption onto hydroxyapatite particles derived from bone meal, which can act as sorbents.

The presence of phosphate in the system may have introduced competitive interactions, as arsenate and phosphate compete for sorption sites on mineral and biomolecular surfaces. This

competition can either enhance or reduce arsenic retention, depending on the relative concentrations and binding affinities of each species (Goldberg & Johnston, 2001). In systems with high phosphate availability, arsenate may be displaced from mineral surfaces, reducing overall immobilisation efficiency. Conversely, under lower phosphate conditions, arsenate incorporation into hydroxyapatite and phosphate minerals may be more favourable. These interactions highlight the complex geochemical behaviour of arsenic and its sensitivity to system-specific factors.

4.1.2. Copper

Although copper exhibited minimal mineralisation, its removal efficiency increased approximately 1.5-fold from T1 to T3, despite consistently low ammonium production. As with arsenic, these results suggest that other geochemical or biochemical mechanisms contributed to metal immobilisation independently of ureolysis. In the case of copper, the increase in pH from T1 to T3, contrary to the pH decline observed for arsenic, further indicates that multiple processes were involved in pH regulation and metal retention.

Copper is known to bind to urease active sites, replacing Ni^{2+} and interfering with enzyme function, which would suppress urea hydrolysis (Zambelli et al., 2011). The low ammonium levels across all treatments and the decrease in precipitate mass from T2 to T3 support this hypothesis, consistent with ureolysis inhibition. However, metal hydrolysis reactions may have contributed to pH increases, particularly the formation of $Cu(OH)_2$ and Cu-hydroxy complexes (Powell et al., 2007; Li et al., 2020). Additionally, copper adsorption onto carboxyl and hydroxyl groups could have altered proton exchange equilibria, further influencing pH dynamics (Witek-Krowiak et al., 2013; Lu et al., 2021).

Calcite precipitation was minimal, with only sparse, minor fibrous-radial calcite crystals observed in T1 and T2, while T3 exhibited no distinct calcite structures and was instead dominated by mass aggregates, suggesting a shift toward poorly crystalline or amorphous sequestration mechanisms. The absence of struvite further supports the idea that inorganic mineralisation was not the primary pathway for copper immobilisation.

Given the suppression of crystalline mineral phases, it is likely that copper immobilisation proceeded via ion exchange, complexation, and surface adsorption onto amorphous or poorly crystalline materials. These disordered phases, which readily form in the presence of organic molecules and when ureolysis is inhibited, offer a high surface area and abundant reactive sites. Li et al. (2014) demonstrated that nanostructured Fe–Cu oxides exhibited enhanced phosphate uptake due to surface adsorption onto amorphous domains, highlighting the sorptive capacity of such materials. Similarly, Czerniczyniec et al. (2007) reported arsenate binding onto biogenic hydroxyapatite with low crystallinity, and Kaur et al. (2023) confirmed that Cu^{2+} can be immobilised via microbially induced precipitation even in the absence of defined mineral phases, through incorporation into amorphous $CaCO_3$ or by surface complexation mechanisms involving organic matrices.

Enzyme-mediated nucleation of these phases is plausible, given the presence of extracellular polymeric substance (EPS)-like components in the crude urease extract, such as proteins, polysaccharides, and polyphenols, as well as organic molecules in the bone meal

solution, including collagen peptides, amino acids, and organic acids. These biomolecules likely act as nucleation centres, stabilising copper within non-crystalline forms through coordination and hydrogen bonding (Shu et al., 2022). The increase in pH from T1 to T3 may have further enhanced the stability of these Cu-organic complexes, favouring copper immobilisation via disordered mineral–organic matrices over well-defined crystalline phases (Li et al., 2020; Lu et al., 2021; Zeng et al., 2025).

4.1.3. Chromium

Cr(III) exhibited decreasing pH, decreasing mass production and crystallinity, consistently low ammonium production, and high removal efficiency (>89.96%). The decline in pH indicates that ureolytic activity was increasingly inhibited with rising Cr(III) concentrations, leading to limited carbonate precipitation. Since ammonium production remained low across all treatments, ureolysis was likely suppressed by Cr(III) binding to urease active sites or interference with ureolytic pathways. Despite reduced mass production, Cr(III) retention remained high, indicating alternative immobilization mechanisms became dominant at higher concentrations.

Cr(III) immobilisation was likely influenced by interactions with carboxyl (-COO^-), hydroxyl (-OH), and phosphate (-PO_4^{3-}) groups, facilitating adsorption onto mineral and organic surfaces. A study by Witek-Krowiak et al. (2013) demonstrated that this process can promote ion exchange of Cr(III) with lighter cations (Ca^{2+}, Mg^{2+}, K^+, H^+), creating localised microenvironments that enhance metal retention. Fourier-transform infrared (FT-IR) spectroscopy studies suggest that interactions between Cr(III) and functional groups cause structural distortions in carbonate phases, consistent with inner-sphere complexation rather than lattice substitution (Rouff, 2012).

Direct substitution of Cr^{3+} for Ca^{2+} in carbonate structures is unlikely due to ionic radius differences (Shannon, 1976). Instead, Cr(III) was more likely retained through surface complexation, adsorption onto interstitial sites within amorphous phases, or precipitation as an alternative solid phase, restricting mobility (Fenter et al., 2022). X-ray absorption fine structure (XAFS) spectroscopy further indicates that Cr(III) in coprecipitation systems would not occupy Ca^{2+} lattice positions but remain as surface-adsorbed $Cr(OH)_3$ or within amorphous carbonate precipitates (Fang et al., 2022).

Another potential Cr(III) immobilisation pathway involved its association with phosphate-rich phases, forming Cr–P interactions that enhanced metal retention (Rouff, 2012). Minor quantities of apatite were identified in the powdered material (2.86% in T1 and 1.25% in T2), although it was absent from the larger crystalline precipitate fractions and from T3. This suggests that phosphate-rich microenvironments may have contributed to Cr(III) immobilisation in the finer fractions, likely via adsorption or incorporation into poorly crystalline phosphate phases. At higher Cr(III) concentrations, however, the dominant retention mechanism appears to shift towards adsorption onto other substrates or precipitation as $Cr(OH)_3$, as phosphate phases were no longer detected in T3. This transition from phosphate-associated retention to hydroxide-driven pathways is consistent with previous studies, which indicate that at lower Cr(III) concentrations (≤20 μM), Cr(III) preferentially interacts with phosphate groups, whereas at elevated concentrations it tends to precipitate as $Cr(OH)_3$ (Fang et al., 2022).

Direct $Cr(OH)_3$ precipitation is a plausible immobilisation mechanism, particularly in environments where carbonate and phosphate buffering capacity maintain conditions favourable for hydroxide formation (Tang et al., 2019). Although no distinct $Cr(OH)_3$ peaks were detected in the PXRD patterns, its presence cannot be entirely ruled out, as it may have formed as an amorphous or poorly crystalline phase below the detection limit, an interpretation supported by prior studies (Fang et al., 2022; Tang et al., 2019). Additionally, functional group interactions with organic molecules, such as proteins and polysaccharides, may have stabilised Cr(III) through complexation, preventing remobilisation and further enhancing sequestration (Gadd et al., 2010).

4.2. Low-impact inhibitors/activators (alkaline domain)

Lead, nickel, cobalt, cadmium, lithium, and zinc were associated with higher pH values, greater variation in removal efficiencies and ammonium production, and sustained mineral precipitation, contrasting with the acidic domain metals. Unlike metals that restricted ureolysis and limited carbonate precipitation, this group facilitated carbonate and phosphate mineralization, influencing metal speciation, solubility, and precipitation pathways. In addition to mineral-driven retention, alternative pathways—including surface complexation, co-precipitation with evolving mineral phases, and interactions with organic ligands— contributed to sequestration and phase transformations. The extent to which each of these mechanisms dominated varied among metals in this group.

4.2.1. Lead

Lead exhibited distinctive behaviour, characterised by the highest and most stable pH values (~9.14–9.16), near-complete removal (>99.78%), and consistent crystal formation across treatments. While lead is a known urease inhibitor—interfering with the enzyme's dinuclear Ni^{2+} active site by displacing coordinated ligands or binding to nearby thiol-containing residues (Amtul et al., 2002; Kataria & Khatkar, 2019)—this inhibition may be attenuated in complex matrices where organic molecules such as proteins or chelating agents sequester Pb^{2+} ions. The high removal efficiency observed suggests multiple concurrent immobilisation pathways, including phosphate precipitation, carbonate co-precipitation, and protein-mediated adsorption.

Immediate turbidity and a chalky appearance observed across all treatments suggest instantaneous supersaturation, leading to the formation of Pb-phosphate colloidal precipitates, initially forming amorphous precipitates that later transform into more stable crystalline phases. Chlorapatite was detected in all treatments indicating an appreciable presence of phosphate phases at lower Pb concentrations, which progressively diminished as carbonate precipitation became more dominant. In urease-driven systems, these phosphates may transition into calcite and other phosphate minerals through sequential chemical and mineralogical processes (Hashimoto et al., 2009). This behaviour aligns with biosorbents such as bone meal and soybean-derived matrices, where ion exchange with Ca^{2+} and Mg^{2+}, surface complexation with hydroxyl, carboxyl, and amino functional groups, and direct precipitation contribute to Pb retention (Liu et al., 2013). The presence of amide ($-NH_2$) and carboxyl ($-COO^-$) groups in protein-based

biomolecules enhances metal chelation, while Pb binding to organic matrices further restricts mobility (Bulgariu et al., 2021).

As the system evolves, initial phosphate phases undergo dissolution and re-precipitation, driven by fluctuations in saturation state and local chemical conditions (Chou et al., 1989). High carbonate availability facilitates calcite nucleation, which may either co-precipitate with or replace phosphate phases depending on ion concentrations and pH stability (Wang et al., 2012). Pb is incorporated into calcite lattices due to its ionic similarity to Ca^{2+}, forming Pb-substituted carbonate structures, further stabilising its immobilisation (Callagon et al., 2014). This dual-phase immobilisation—where Pb transitions between phosphate and carbonate phases—is critical in alkaline environments, as it minimises re-solubilisation and enhances long-term stability. Organic molecules also mediate these transformations, directing crystal growth and stabilising intermediate phases by altering nucleation kinetics (Dupraz et al., 2009). The low ammonium levels observed in the system likely reflect a balance between moderate ureolytic production and concurrent immobilisation processes—such as incorporation into struvite, enzyme encapsulation, or early carbonate saturation—rather than simply indicating limited urease activity.

Crystallisation patterns further suggest concentration-dependent saturation effects. At lower Pb concentrations (T1, T2), undersaturation favours controlled nucleation and growth, producing well-defined crystals ranging from 0.10 to 0.50 mm. In contrast, higher Pb concentrations (T3) induce supersaturation, promoting rapid nucleation and the formation of fine aggregates due to intense competition for carbonate ions. Additionally, Pb binding to crystal surfaces disrupts ordered mineral development, further influencing morphology (Fiorito et al., 2022). Such disruptions are frequently observed in protein-mediated mineralisation systems, where organic ligands influence crystal habit and growth directionality (Evans, 2020). Together, the strength of Pb-phosphate and Pb-carbonate interactions and the role of organic biomolecules underscore a multifaceted immobilisation process involving precipitation, adsorption, and biomolecular entrapment

4.2.2. Lithium

Due to its monovalent charge and weak binding affinity for urease cofactors such as Ni^{2+}, lithium appears to have a negligible effect on urease activity in all treatments. As a result, urease activity remains stable, ensuring uninterrupted carbonate dynamics and favouring calcite precipitation. This is reflected in consistently high ammonium production (79.63% to 85.97%) across treatments, which indicates robust urease activity, drives urea hydrolysis, and provides a steady supply of carbonate ions for precipitation.

Lithium promotes characteristic calcite precipitation patterns due to stable pH conditions and limited competition for binding sites. Across treatments, pH remains stable with a modest increase in precipitate mass, while lithium removal efficiency declines from T1 to T3. This trend may reflect lithium's weak interaction with mineral surfaces: its high solubility promotes rapid nucleation, but limited affinity for the crystal lattice results in poor incorporation and predominant surface adsorption (Füger et al., 2019).

In lithium treatments, calcite crystals exhibit a broad size distribution in T1, progressively narrowing in T2 and T3. XRD diffractograms and micromorphological analysis reflect a reduction in crystallinity from T1 to T3. Lithium ions may be adsorbed at low concentrations onto calcite surfaces without significantly modifying crystal growth patterns. However, at higher concentrations, lithium interferes with step-edge attachment sites (Pastero et al., 2004), increasing nucleation rates while limiting overall crystal growth, leading to the fibrous calcite structures observed in T3, as lithium alters the energy barriers associated with nucleation and growth. This behaviour aligns with studies on alkali metal interactions with carbonate minerals, where lithium has been observed to modify crystal habit by promoting one-dimensional over two-dimensional faceted growth (Gu et al., 2024).

Diffractograms confirm high calcite proportions in lithium treatments, increasing from 91.2% in T1 to 93.6% in T2, with struvite content decreasing correspondingly from 8.8% to 6.4%. This trend suggests that lithium promotes calcite precipitation while inhibiting struvite formation. Lithium's relatively small ionic radius (0.76 Å) and strong hydration energy reduce its ability to incorporate into phosphate-based minerals like struvite. Unlike magnesium, which stabilizes the struvite lattice, lithium interacts weakly with phosphate ions, making its incorporation into struvite energetically unfavourable. Instead, lithium weakly adsorbs onto calcite surfaces, further reinforcing its role in promoting carbonate precipitation over phosphate mineralization (Pastero et al., 2004). Although lithium does not directly contribute to phosphate mineralisation, Rietveld refinement revealed the presence of chlorapatite in T1 (3.11%) and T2 (2.67%) as minor accessory phases. These likely formed through localised supersaturation of calcium and phosphate ions released from bone meal under alkaline conditions sustained by ureolysis.

The narrowing crystal size range in T3 and reduced removal efficiency suggest that higher lithium concentrations promote rapid nucleation but limit crystal growth, reducing lithium incorporation into mineral phases. Its weak coordination with organic ligands in the system further ensures that carbonate dynamics remain unaffected. (Fulfer *et al.*, 2025).

4.2.3. Nickel and cobalt

Nickel and cobalt exhibit similar trends, with both metals showing pH decline and decreasing ammonium production as their concentrations increase. Nickel, a native cofactor for urease, can lead to allosteric inhibition or oversaturation of binding sites when present in excess, disrupting enzyme activity. Cobalt, like nickel, interacts with urease and may inhibit its activity through direct binding to essential cofactors, leading to reduced enzymatic efficiency. This interference leads to progressive suppression of ureolysis, limiting carbonate formation and subsequently affecting mineralisation (Singh et al., 2017). However, metal-binding peptides and proteins, particularly metallothionein and glutathione, may reduce the free concentration of Ni^{2+} and Co^{2+} in solution, potentially modulating urease inhibition (Balzano et al., 2020).

Despite this inhibition, removal efficiency increases across treatments, suggesting the involvement of secondary immobilisation mechanisms, particularly metal-phosphate complex formation. Nickel and cobalt react with phosphate ions released from bone meal or enzymatic phosphatase activity, forming nickel phosphate ($Ni_3(PO_4)_2$) and cobalt phosphate ($Co_3(PO_4)_2$)

during mineralisation (Liu et al., 2017). Nickel phosphate crystallises directly, whereas cobalt phosphate initially forms an amorphous precursor before transitioning into a crystalline phase, influenced by biomolecules that stabilise amorphous cobalt phases before crystallisation (Hövelmann et al., 2019; Karafiludis et al., 2022). Rietveld refinement revealed the presence of chlorapatite in both nickel and cobalt treatments, with decreasing proportions from T1 to T3 (Ni: 4.31%, 2.04%, 1.76%; Co: 2.7%, 0.9%, 0%). This trend suggests that apatite formation occurred under conditions of high phosphate and calcium availability at lower metal concentrations but was progressively suppressed at higher concentrations. In these environments, competitive pathways—such as the direct precipitation of metal-specific phosphates (e.g., $Ni_3(PO_4)_2$, $Co_3(PO_4)_2$) or incorporation into struvite—likely dominated phosphate immobilisation as metal concentrations increased. The formation of chlorapatite under lower metal loadings indicates that calcium-phosphate precipitation was a relevant immobilisation route, particularly when carbonate saturation and urease inhibition were moderate. At higher concentrations, enhanced urease suppression, increased carbonate precipitation, or preferential binding of phosphate to metal ions likely limited apatite nucleation.

Nickel and cobalt exhibit distinct behaviours in carbonate precipitation. Nickel is primarily retained through surface adsorption onto calcite rather than lattice incorporation, modifying crystal morphology without significant structural incorporation. In contrast, cobalt disrupts calcite formation by introducing structural distortions, favouring amorphous or alternative carbonate phases instead of direct lattice substitution (Parigi et al., 2022; Lakshtanov & Stipp, 2007). These differences are influenced by biomolecules, as metal-binding proteins and peptides stabilise amorphous phases for cobalt, delaying crystallisation, whereas nickel's stronger interaction with phosphate groups leads to earlier and more structured precipitation (Karafiludis et al., 2022; Reddy & Prasad, 1990).

In struvite formation, nickel incorporates directly into the lattice as Ni-struvite ($NH_4NiPO_4{\cdot}6H_2O$) without requiring an amorphous precursor. In contrast, cobalt follows a two-step process, first forming an amorphous precursor before crystallising into Co-struvite or cobalt phosphate; biomolecules also contribute to this two-step mechanism in an analogous way to the calcite, by stabilising amorphous cobalt phases before they transition into crystalline structures, affecting nucleation and growth dynamics (Karafiludis et al., 2022).

Nickel precipitate mass peaks at T2 before declining in T3, while cobalt precipitation continues increasing from T1 to T3, reflecting differences in mineral transformation pathways. Increased urease inhibition at higher Ni^{2+} concentrations may have reduced carbonate availability for precipitation, alongside competition with other ions and changes in mineral saturation dynamics. In contrast, cobalt maintains phosphate-dominated precipitation pathways, further distinguishing its mineralisation behaviour (Singh et al., 2017). Metal-binding proteins modulate these precipitation trends, particularly in biomolecule-rich environments (Yaashikaa et al., 2024).

4.2.4 Cadmium and Zinc

Cadmium demonstrates a stable, slightly increasing trend in pH and ammonium production from T1 to T3, accompanied by a consistent rise in precipitate mass and metal

immobilisation efficiency. Although cadmium has been shown to inhibit urease activity at concentrations exceeding 50 μM this inhibition becomes more pronounced at higher concentrations, such as 500 μM, likely due to its high affinity for sulfhydryl (-SH) and histidine residues at the enzyme's active site (Kaur et al., 2023). These interactions disrupt the coordination of essential Ni^{2+} ions and impair enzymatic catalysis, mirroring the mechanism observed for thiol- and histidine-targeting inhibitors like Ag^{+} and N-phenylmaleimide (Svane et al., 2020). However, biomolecules from bone meal and soybean-derived materials likely mitigate this effect by complexing with Cd^{2+}, reducing its free-ion activity. The sustained ammonium production suggests that urease-mediated urea hydrolysis remains active, supporting continuous carbonate formation. Additionally, metallothioneins and phytochelatins, which bind Cd^{2+}, may further reduce free-ion activity, thus minimizing urease inhibition and promoting precipitation pathways.

Crystallographic analysis indicates that cadmium consistently incorporates into crystalline mineral phases across treatments, forming cadmium carbonate (otavite) or cadmium phosphate; Cd^{2+} can substitute for Ca^{2+} in calcite, forming a stable Cd-Ca solid solution, or undergo chemisorption onto calcite surfaces, influencing precipitation efficiency (Kaur et al., 2023). The precipitation pathway depends on phosphate availability: in carbonate-rich systems, Cd forms cadmium carbonate, while in phosphate-rich environments, Cd initially forms amorphous cadmium phosphate, which later transitions into crystalline structures (Guo et al., 2023). The high phosphate content in bone meal may further promote cadmium-phosphate formation, while organic molecules in soybean-derived biomaterials contribute to Cd immobilisation through adsorption and chelation mechanisms. Crystallographic analysis identified hydroxyapatite at 8.5% in T1 and 1.2% in T2, with no detectable presence in T3, indicating that phosphate-mediated immobilisation dominated at lower cadmium concentrations but progressively gave way to carbonate-driven pathways as phosphate availability or precipitation kinetics shifted.

While Cd^{2+} does not significantly affect phosphate removal efficiency, it alters struvite crystallisation. At low concentrations, Cd^{2+} integrates into struvite without disrupting its structure, but at higher concentrations, it destabilises crystallisation, promoting the formation of amorphous phases and inhibiting the nucleation of well-defined crystals (Saidou et al., 2015; Korchef et al., 2023; Guo et al., 2023). The parallel trends of increasing removal efficiency and consistent crystallinity indicate a well-regulated mineralisation process. However, crystal morphology evolves across treatments: T1 exhibits a diverse range of forms (0.10–0.50 mm, including spherical, globular, star-shaped, and dumbbell-like structures), whereas T3 predominantly features spherical and globular forms. Higher Cd^{2+} concentrations promote rapid nucleation, reducing morphological diversity and favouring simpler crystal shapes.

Zinc exhibits a stable but slightly decreasing pH from T1 to T3, indicating mild urease inhibition at higher concentrations, likely due to Zn^{2+} binding to urease's active site, which reduces urea hydrolysis and ammonium production (Zambelli et al., 2011; Svane et al., 2020). Despite this, precipitate mass steadily increases across treatments, suggesting secondary immobilisation mechanisms such as coprecipitation or mixed-metal mineral phase formation. Zinc's coordination with biomolecules, particularly histidine, glutamate, and cysteine, likely

affects calcite incorporation, struvite formation, and phosphate precipitation by stabilizing amorphous phases and influencing mineralisation pathways.

Zinc mineralisation patterns reveal that Zn is incorporated into calcite primarily through ion substitution with Ca^{2+}, forming a solid solution with smithsonite ($ZnCO_3$) at low concentrations. XRD analysis confirmed that calcite remained the dominant phase across all treatments, consistently representing over 90% of the precipitate mass, while no apatite or other phosphate phases were detected. Zn initially adsorbs as a tetrahedral complex on calcite surfaces but transitions into octahedral coordination upon full lattice incorporation (Mavromatis et al., 2019). However, at higher Zn concentrations, strain effects in the calcite lattice reduce Zn incorporation efficiency (Cheng et al., 1998; Wang et al., 2021).

Zinc's interaction with struvite varies with concentration. At low Zn^{2+} levels (≤5 μM), Zn adsorbs onto struvite surfaces as octahedral and tetrahedral complexes, slightly distorting the crystal lattice. However, at ≥50 μM, Zn integration into struvite declines in favour of separate Zn-phosphate precipitates (Rouff & Juarez, 2014, Lu et al., 2021). This shift alters struvite morphology, producing smaller crystals (0.20–0.50 mm) and increasing overall struvite content to 16.2% in T3, according to XRD analysis. Calcite crystals also remain small (0.05–0.30 mm), with the smallest appearing in T3. Diffractograms show sharper peaks at T2, indicating favourable conditions for Zn crystallisation at intermediate concentrations, but peak intensity declines at T3 due to supersaturation effects (Brazier et al., 2024; Wang et al., 2021).

Competitive interactions with phosphate and other metal ions influence zinc coprecipitation. In mixed-metal systems containing Zn and Cu, Zn preferentially binds to phosphate, increasing Zn-phosphate precipitation while suppressing Cu-phosphate formation. This competition suggests that Zn's strong affinity for phosphate alters mineralisation pathways and reduces its retention within struvite at high concentrations. No apatite-group minerals were identified in any of the zinc treatments, despite the presence of phosphate in the system. This absence can be attributed to the strong affinity of Zn^{2+} for phosphate, which promotes the rapid formation of amorphous zinc phosphate phases. These interactions likely sequester phosphate before apatite nucleation can occur and alter local saturation conditions, making them unfavourable to the slow and ordered crystallisation pathway required for apatite formation. Instead, mineralisation proceeds via alternative routes, including amorphous Zn–phosphate complexes and carbonate-based immobilisation.

In cadmium treatments, hydroxyapatite was detected at 4.37% in T1 and 1.27% in T2 but was absent in T3. The formation of apatite in cadmium treatments and its absence in zinc reflects the sensitivity of phosphate mineralisation pathways to the balance between Ca^{2+}, PO_4^{3-}, and the target metal. In cadmium systems, apatite formed under conditions of high calcium and phosphate availability, where phosphate was not yet fully sequestered by cadmium. As Cd^{2+} concentrations increased, phosphate was increasingly directed towards the formation of cadmium carbonate or cadmium phosphate phases, progressively suppressing apatite formation. In zinc systems, by contrast, the formation of amorphous phosphate phases and the preferential binding of Zn^{2+} to PO_4^{3-}—likely driven by its high affinity and rapid complexation—limited the availability of phosphate for apatite nucleation, thereby inhibiting the development of this phase even under favourable chemical conditions.

5. Conclusions

This study demonstrated that Enzyme-Mediated Multiphase Precipitation (EMMP) is an effective metal immobilization strategy, achieving high removal efficiencies for most tested EMs. Removal rates exceeded 95% for lead, cadmium, and lithium and 80% for cobalt, nickel, zinc, and chromium whereas arsenic, and copper exhibited lower removal efficiencies, likely due to their inhibitory effects on enzymatic and precipitation pathways. The relative immobilization efficiency followed the sequence: Pb > Cd > Li > Cr > Zn > Co > Ni > Cu > As based on mean removal across treatments, underscoring the differential responses of metals within the EMMP system.

The primary immobilization pathway was governed by the ureolytic process, wherein urease catalyses urea hydrolysis, generating ammonium and carbonate. This reaction promoted the formation of calcite, struvite and accessory phases, enabling both direct precipitation of metal carbonates and co-precipitation within evolving mineral phases. However, secondary mechanisms—including ion exchange, surface adsorption, and biomolecule-mediated interactions—further enhanced metal retention by stabilizing intermediates and expanding the range of immobilization pathways beyond carbonate mineralization. Notably, in several treatments, metal immobilisation increased despite lowered precipitate mass, suggesting the significant contribution of biosorption and direct lattice incorporation mechanisms under metal-rich conditions. Direct phosphate precipitation also played a key role in immobilising certain metals, particularly lead, where phosphate precursors influenced the crystallogenesis of both calcite and struvite phases. This mechanistic complementarity expands the range of conditions under which EMMP remains effective.

Additionally, ammonium mitigation occurred through multiple, concurrent pathways, including incorporation into mineral structures such as struvite and metal-substituted struvite, adsorption onto mineral surfaces, and complexation with biomolecules present in the crude urease extract. The differences in ammonium concentrations across treatments—highest in the lithium and zinc systems, moderate in cadmium, nickel, and cobalt, and lowest in the presence of chromium, copper, lead, and arsenic—were driven by the combined effects of these mitigation mechanisms and metal-specific urease inhibition, as well as variations in phosphate and metal availability, mineral phase formation, and pH-dependent equilibria. Importantly, EMMP demonstrated efficacy even under mildly acidic conditions (pH ~5.0), traditionally unfavourable for urea hydrolysis, indicating that the crude extract retains partial catalytic function in such environments. This integrated performance reinforces EMMP's role as a comprehensive solution for both metal and nitrogen management.

While this study examined a wide array of EMs, it primarily focused on their individual behaviours rather than their interactions within complex multi-metal systems. However, real-world contaminated environments typically contain mixtures of metals that can influence each other's precipitation and immobilization dynamics. For instance, arsenic strongly inhibited crystallization, which may impact the effectiveness of EMMP when applied to mixed-metal contamination scenarios. Future research should investigate metal–metal interactions within EMMP systems to determine whether competitive inhibition, synergistic effects, or preferential precipitation pathways emerge in multi-contaminant settings. Understanding these interactions

will be essential for optimizing EMMP performance in real-world applications and ensuring its reliability as a remediation strategy.

Additionally, while this study investigated EMMP in aqueous systems, its effectiveness in soil environments remains to be fully explored. The presence of soil minerals, organic matter, and varying geochemical conditions could influence precipitation pathways, metal immobilization efficiency, and long-term stability. Future research should focus on applying EMMP to contaminated soils, assessing its interactions with soil matrices, and evaluating potential limitations or enhancements that arise from soil heterogeneity, porosity, and microbial activity. These insights will be critical for translating EMMP from controlled laboratory conditions to large-scale field applications.

Beyond its remediation potential, EMMP aligns with circular economy principles and the GHG Protocol by utilizing food waste-derived enzymes and mineral waste sources. It offers a low-energy, sustainable alternative to conventional chemical precipitation methods. Its ability to enhance metal sequestration while minimizing greenhouse gas emissions supports broader environmental applications, including contaminated soil stabilization and wastewater treatment.

To enhance the applicability of EMMP, future research should focus on three key aspects: improving mechanistic understanding by identifying the specific enzymes and biochemical interactions responsible for secondary immobilization pathways; assessing the long-term stability of immobilized metals under variable environmental conditions, including pH fluctuations, redox changes, and biological activity; and validating large-scale applications through field trials to refine process parameters and assess feasibility in diverse contamination scenarios. Additionally, it is essential to evaluate potential by-products of the process, particularly the concentrations of calcium, magnesium, iron, manganese, bromate, chlorine, and other compounds in treated water, to ensure compliance with water quality standards and mitigate unintended environmental impacts.

Overall, this study underscores the versatility of EMMP under controlled laboratory conditions as an innovative, multifunctional biogeotechnical approach for heavy metal immobilization and ammonium mitigation, with strong potential for scalable environmental applications.

CRediT authorship contribution statement

Jaime Toney: Writing – review & editing, Supervision, Visualization, Validation, Project administration, Formal analysis, Resources, Funding acquisition. **John MacDonald:** Writing – review & editing, Supervision, Visualization, Validation, Project administration, Formal analysis, Resources, Funding Acquisition. **Heloisa Dickinson:** Writing – Original draft, Visualization, Software, Methodology, Investigation, Formal analysis, Data curation, Conceptualization.

Declaration of competing interest

The authors declare that they have no known competing financial interests or personal relationships that could have appeared to influence the work reported in this paper.

Acknowledgement

The authors thank Dr. Connor Brolly from the University of Glasgow for their support with the ICP-OES analyses and Liene Spruzeniece of the Geoanalytical Electron Microscopy and Spectroscopy (GEMS) facility at the University of Glasgow for her support and assistance in this work. We are also grateful to Dr. Gavin Sim from the University of Edinburgh for performing the ammonium analysis. This research was fully funded by the GALLANT project – UKRI-NERC GALLANT – under grant reference NERC-NE/W005042/1.

Data availability

The authors declare that the data supporting the findings of this study are available within the paper and in the Supplementary section. Should any raw data files be needed in another format they are available from the corresponding author upon reasonable request.

Appendix A. Supplementary data

[Hyperlink]

References

Ahenkorah, I., Rahman, M.M., Karim, M.R. & Beecham, S. (2021) Enzyme induced calcium carbonate precipitation and its engineering application: a systematic review and meta-analysis. *Construction and Building Materials*, 308, 125000. https://doi.org/10.1016/j.conbuildmat.2021.125000

Ajsuvakova, O.P., Tinkov, A.A., Aschner, M., Rocha, J.B.T., Michalke, B., Skalnaya, M.G., Skalny, A.V., Butnariu, M., Dadar, M., Sarac, I., Aaseth, J. & Bjørklund, G. (2020) Sulfhydryl groups as targets of mercury toxicity. *Coordination Chemistry Reviews*, 417, 213343. https://doi.org/10.1016/j.ccr.2020.213343

Almajed, A.A. (2017) *Enzyme induced carbonate precipitation (EICP) for soil improvement*. PhD thesis, Arizona State University. ProQuest Dissertations & Theses, 10615077.

Almajed, A., Abbas, H., Arab, M., Alsabhan, A., Hamid, W. & Al-Salloum, Y. (2020) Enzyme-induced carbonate precipitation (EICP)-based methods for ecofriendly stabilization of different types of natural sands. *Journal of Cleaner Production*, 274, 122627. https://doi.org/10.1016/j.jclepro.2020.122627

Amtul, Z., Atta-ur-Rahman, Siddiqui, R.A. & Choudhary, M.I. (2002) Chemistry and mechanism of urease inhibition. *Current Medicinal Chemistry*, 9, 1323–1348.

Arab, M.G., Alsodi, R., Almajed, A., Yasuhara, H., Zeiada, W. & Shahin, M.A. (2021) State-of-the-art review of enzyme-induced calcite precipitation (EICP) for ground improvement: applications and prospects. *Geosciences*, 11, 492. https://doi.org/10.3390/geosciences11120492

Arai, Y. & Sparks, D.L. (2002) Residence time effects on arsenate surface speciation at the aluminum oxide–water interface. *Soil Science Society of America Journal*, 66(3), 773–782.

Avramenko, M., Nakashima, K., Takano, C. and Kawasaki, S., *Enzymatically mediated precipitation of calcium phosphate compounds: a promising approach for sustainable soil enhancement*, in *Proceedings of the XVIII European Conference on Soil Mechanics and Geotechnical Engineering (ECSMGE 2024)*, Edinburgh: Taylor & Francis, 2024. doi:10.1201/9781003431749-393.

Balzano, S., Sardo, A., Blasio, M. et al. (2020) Microalgal metallothioneins and phytochelatins and their potential use in bioremediation. *Frontiers in Microbiology*.

Behera, S.N., Sharma, M., Aneja, V.P. & Balasubramanian, R. (2013) Ammonia in the atmosphere: a review on emission sources, atmospheric chemistry and deposition on terrestrial bodies. *Environmental Science and Pollution Research*, 20(11), 8092–8131. https://doi.org/10.1007/s11356-013-2051-9

Beaufils, C., Man, H.-M., de Poulpiquet, A., Mazurenko, I. & Lojou, E. (2021) From enzyme stability to enzymatic bioelectrode stabilization processes. *Catalysts*, 11(4), 497. https://doi.org/10.3390/catal11040497

Bian, Y., Chen, Y., Zhan, L., Guo, H., Ke, H., Wang, Y., Wang, Q., Gao, Y. & Gao, Y. (2024) Effects of enzyme-induced carbonate precipitation technique on multiple heavy metals immobilization and unconfined compressive strength improvement of contaminated sand. *Science of the Total Environment*, 947, 174409. https://doi.org/10.1016/j.scitotenv.2024.174409

Borch, T. et al. (2010) Biogeochemical redox processes and their impact on contaminant dynamics. *Environmental Science & Technology*, 44(1), 15–23.

Bulgariu, D. & Bulgariu, L. (2018) Potential use of alkaline treated algae waste biomass as sustainable biosorbent for clean recovery of cadmium(II) from aqueous media: batch and column studies. *Journal of Cleaner Production*, 171, 339–349.

Bulgariu, L. et al. (2001) Equilibrium and kinetics studies of heavy metal ions biosorption on green algae waste biomass. *Bioresource Technology*, 103(10), 4897–4906.

Bulgariu, L., Ferţu, D.I., Cara, I.G. & Gavrilescu, M. (2021) Efficacy of alkaline-treated soy waste biomass for the removal of heavy-metal ions and opportunities for their recovery. *Materials*, 14(23), 7413. https://doi.org/10.3390/ma14237413

Brazier, J.-M., Goetschl, K.E., Dietzel, M. and Mavromatis, V., 2024. Effect of mineral growth rate on zinc incorporation into calcite and aragonite. *Chemical Geology*, 643, 121821. https://doi.org/10.1016/j.chemgeo.2023.121821

Cao, R.X., Ma, L.Q., Chen, M., Singh, S.P. & Harris, W.G. (2003) Phosphate-induced metal immobilization in a contaminated site. *Environmental Pollution*, 122(1), 19–28. https://doi.org/10.1016/S0269-7491(02)00283-X

Callagon, E., Fenter, P., Nagy, K.L. & Sturchio, N.C. (2014) Incorporation of Pb at the calcite (104)-water interface. *Environmental Science & Technology*, 48(16), 9263–9269. https://doi.org/10.1021/es5014888

Cheng, L., Sturchio, N.C., Woicik, J.C., Kemner, K.M., Lyman, P.F. & Bedzyk, M.J., 1998. High-resolution structural study of zinc ion incorporation at the calcite cleavage surface. *Surface Science*, 415, pp.L976–L982.

Chirakkara, R.A., Cameselle, C. & Reddy, K.R. (2016) Assessing the applicability of phytoremediation of soils with mixed organic and heavy metal contaminants. *Reviews in Environmental Science and Bio/Technology*, 15, 299–326. https://doi.org/10.1007/s11157-016-9391-0

Chou, L. et al. (1989) Comparative study of the kinetics and mechanisms of dissolution of carbonate minerals. *Chemical Geology*, 78(3–4), 269–282.

Crane, L., Ray, H., Hamdan, N. & Boyer, T.H. (2022) Enzyme-induced carbonate precipitation utilizing fresh urine and calcium-rich zeolites. *Journal of Environmental Chemical Engineering*, 10(2), 107238. https://doi.org/10.1016/j.jece.2022.107238

Czerniczyniec, M., Farías, S., Magallanes, J. & Cicerone, D. (2007) Arsenic(V) adsorption onto biogenic hydroxyapatite: solution composition effects. *Water, Air, and Soil Pollution*, 180, 75–82. https://doi.org/10.1007/s11270-006-9251-6

DeJong, J.T. et al. (2010) Bio-mediated soil improvement. *Ecological Engineering*, 36(2), 197–210.

Döbelin, N., Kleeberg, R., „Profex: a graphical user interface for the Rietveld refinement program *BGMN*„, Journal of Applied Crystallography 48 (2015), 1573-1580. doi:10.1107/S1600576715014685

Dorozhkin, S.V. (2012) Calcium orthophosphate-based bioceramics. *Materials*, 5(12), 2749–2794.

Dupraz, C. et al. (2009) Processes of carbonate precipitation in modern microbial mats. *Earth-Science Reviews*, 96(3–4), 141–162.

Evans, J.S. (2020) Glycosylation: a “last word” in the protein-mediated biomineralization process. *Crystals*, 10(9), 818. https://doi.org/10.3390/cryst10090818

FAO (2024) *FAOSTAT statistical database*. Rome: Food and Agriculture Organization of the United Nations. https://www.fao.org/faostat/en/

Fang, Z., Liu, W., Yao, T., Zhou, G., Wei, S. & Qin, L. (2022) Experimental study of chromium (III) coprecipitation with calcium carbonate. *Geochimica et Cosmochimica Acta*, 322, 94–108. https://doi.org/10.1016/j.gca.2022.02.010

Farghali, M., Chen, Z., Osman, A.I. et al. (2024) Strategies for ammonia recovery from wastewater: a review. *Environmental Chemistry Letters*, 22, 2699–2751. https://doi.org/10.1007/s10311-024-01768-6

Fenter, P. et al. (2022) Mineral–water interfacial structures revealed by synchrotron X-ray scattering. *Progress in Surface Science*, 97(2), 100635.

Fiorito, L., Fracassi, C., Passiu, C. et al. (2022) Lead removal from aqueous solutions by calcite: surface reactions and precipitation mechanisms studied by XPS, SEM-EDS, XRPD and FTIR. *Journal of Hazardous Materials*, 424, 127411.

Fulfer, K.D., Galle Kankanamge, S.R., Chen, X., Woodard, K.T. & Kuroda, D.G. (2025) Elucidating the mechanism behind the infrared spectral features and dynamics observed in the carbonyl stretch region of organic carbonates interacting with lithium ions. *Journal of Chemical Physics*, [early access]. https://doi.org/10.1063/5.0049742

Füger, A., Konrad, F., Leis, A., Dietzel, M. & Mavromatis, V. (2019) Effect of growth rate and pH on lithium incorporation in calcite. *Geochimica et Cosmochimica Acta*, 248, 14–24.

Gadd, G.M. (2010) Metals, minerals and microbes: geomicrobiology and bioremediation. *Microbiology*, 156(3), 609–643.

Gebauer, D. et al. (2014) Pre-nucleation clusters as solute precursors in crystallisation. *Chemical Society Reviews*, 43(7), 2348–2371.

Goldberg, S. & Johnston, C.T. (2001) Mechanisms of arsenic adsorption on amorphous oxides evaluated using macroscopic measurements, vibrational spectroscopy, and surface complexation modeling. *Journal of Colloid and Interface Science*, 234(1), 204–216.

Gong, P., Li, C., Yi, Q., Gao, X., Dai, C., Du, J., Liu, J., Zhang, X., Duan, Y., Tan, T. & Kong, S. (2022) Enhanced adsorption of inorganic arsenic by Mg-calcite under circumneutral conditions. *Geochimica et Cosmochimica Acta*, 335, 85–97. https://doi.org/10.1016/j.gca.2022.08.031

Gowthaman, S., Mohsenzadeh, A., Nakashima, K. & Kawasaki, S. (2022) Removal of ammonium by-products from the effluent of bio-cementation system through struvite precipitation. *Materials Today: Proceedings*, 61(Part 2), 243–249. https://doi.org/10.1016/j.matpr.2021.09.013

Gowthaman, S., Yamamoto, M., Chen, M., Nakashima, K. & Kawasaki, S. (2023) Baseline investigation on enzyme induced calcium phosphate precipitation for solidification of sand. *Frontiers in Built Environment*, 9. https://doi.org/10.3389/fbuil.2023.1307650

Gu, K., Feng, W., Wei, H. & Dang, L. (2024) The factors influencing lithium carbonate crystallization in spent lithium-ion battery leachate. *Processes*, 12(4), 753. https://doi.org/10.3390/pr12040753

Guo, J., Wu, S., Zhang, X., Xie, H., Chen, F., Yang, Y. & Zhu, R. (2023) The fate of Cd during the replacement of Cd-bearing calcite by calcium phosphate minerals. *Environmental Pollution*, 316(Part 1), 120491. https://doi.org/10.1016/j.envpol.2022.120491

Gupta, A. & Balomajumder, C. (2015) Simultaneous adsorption of Cr(VI) and phenol onto tea waste biomass from binary mixture: multicomponent adsorption, thermodynamic and kinetic study. *Journal of Environmental Chemical Engineering*, 3(2), 785–796. https://doi.org/10.1016/j.jece.2015.03.003

Gomez, M.G., Martinez, B.C., DeJong, J.T., Hunt, C.E., deVlaming, L.A., Major, D.W. & Dworatzek, S.M. (2015) Field-scale bio-cementation tests to improve sands. *Proceedings of the Institution of Civil Engineers – Ground Improvement*, 168(3), 206–216. https://doi.org/10.1680/grim.13.00052

Hamdan, N. & Kavazanjian, E. (2016) Enzyme-induced carbonate mineral precipitation for fugitive dust control. *Géotechnique*, 66(7), 546–555. https://doi.org/10.1680/jgeot.15.P.168

Han, L.-J., Li, J.-S., Xue, Q., Guo, M.-Z., Wang, P. & Poon, C.S. (2022) Enzymatically induced phosphate precipitation (EIPP) for stabilization/solidification (S/S) treatment of heavy metal tailings. *Construction and Building Materials*, 314(Part A), 125577. https://doi.org/10.1016/j.conbuildmat.2021.125577

Hashimoto, Y., Takaoka, M., Oshita, K. & Tanida, H. (2009) Incomplete transformations of Pb to pyromorphite by phosphate-induced immobilization investigated by X-ray absorption fine

structure (XAFS) spectroscopy. *Chemosphere*, 76(5), 616–622. https://doi.org/10.1016/j.chemosphere.2009.04.049

Huang, Y. et al. (2014) Functional group interactions in biosorption. *Journal of Hazardous Materials*, 264, 1–8.

Hövelmann, J., Putnis, A., Geisler, T. & Schmidt, B.C. (2019) Struvite crystallisation and the effect of Co^{2+} ions. *Mineralogical Magazine*, 83(3), 317–329.

IPCC (2022) *Climate change 2022: impacts, adaptation and vulnerability*. Geneva: Intergovernmental Panel on Climate Change.

Jiang, L., Liu, X., Yin, H., Liang, Y., Liu, H., Miao, B., Peng, Q., Meng, D., Wang, S., Yang, J. & Guo, Z. (2020) The utilization of biomineralization technique based on microbial induced phosphate precipitation in remediation of potentially toxic ions contaminated soil: a mini review. *Ecotoxicology and Environmental Safety*, 191, 110009. https://doi.org/10.1016/j.ecoenv.2019.110009

Karafiludis, D., Borrmann, T., Cipriano, L.A., Hövelmann, J., Prieto, M. & Putnis, A. (2022) Ni- and Co-struvites: revealing crystallization mechanisms and crystal engineering toward applicational use of transition metal phosphates. *Crystal Growth & Design*, 22(12), 7365–7377. https://doi.org/10.1021/acs.cgd.2c00963

Kataria, R. & Khatkar, A. (2019) Lead molecules for targeted urease inhibition: an updated review from 2010–2018. *Current Protein and Peptide Science*, 20(12), 1158–1188. https://doi.org/10.2174/1389203720666190320170215

Kaur, M., Sidhu, N. & Reddy, M.S. (2023) Removal of cadmium and arsenic from water through biomineralization. *Environmental Monitoring and Assessment*, 195, 1019. https://doi.org/10.1007/s10661-023-11616-9

Korchef, A., Abouda, S. & Souid, I. (2023) Optimizing struvite crystallization at high stirring rates. *Crystals*, 13, 711. https://doi.org/10.3390/cryst13040711

Krajewska, B. (2019) Urease-aided calcium carbonate mineralization for engineering applications: a review. *Journal of Advanced Research*, 18, 7–17.

Kumari, P., Sharma, P., Srivastava, S. & Srivastava, M.M. (2005) Arsenic removal from the aqueous system using plant biomass: a bioremedial approach. *Journal of Industrial Microbiology & Biotechnology*, 32(11–12), 521–526. https://doi.org/10.1007/s10295-005-0042-7

Lai, H., Ding, X., Cui, M., Zheng, J., Chen, Z., Pei, J. & Zhang, J. (2023) Mechanisms and influencing factors of biomineralization-based heavy metal remediation: a review. *Biogeotechnics*, 1(3), 100039. https://doi.org/10.1016/j.bgtech.2023.100039

Lakshtanov, L.Z. & Stipp, S.L.S. (2007) Experimental study of nickel(II) interaction with calcite: adsorption and coprecipitation. *Geochimica et Cosmochimica Acta*, 71(15), 3686–3697. https://doi.org/10.1016/j.gca.2007.04.017

Lee, Y.J., Stephens, P.W., Tang, Y., Li, W., Phillips, B.L., Parise, J.B. & Reeder, R.J. (2009) Arsenate substitution in hydroxylapatite: structural characterization of the $Ca_5(P_xAs_{1-x}O_4)_3OH$ solid solution. *American Mineralogist*, 94, 666–675. https://doi.org/10.2138/am.2009.3120

Li, G., Gao, S., Zhang, G. & Zhang, X. (2014) Enhanced adsorption of phosphate from aqueous solution by nanostructured iron(III)–copper(II) binary oxides. *Chemical Engineering Journal*, 235, 124–131.

Li, X., Azimzadeh, B., Martinez, C.E. & McBride, M.B. (2021) Pb mineral precipitation in solutions of sulfate, carbonate and phosphate: measured and modeled Pb^{2+} solubility and Pb^{2+} activity. *Minerals*, 11(6), 620. https://doi.org/10.3390/min11060620

Li, X. et al. (2020) Co-precipitation with $CaCO_3$ to remove heavy metals and significantly reduce the moisture content of filter residue. *Chemosphere*, 239, 124660. https://doi.org/10.1016/j.chemosphere.2019.124660

Liu, D., Li, Z., Li, W., Zhong, Z., Xu, J., Ren, J. & Ma, Z. (2013) Adsorption behavior of heavy metal ions from aqueous solution by soy protein hollow microspheres. *Industrial & Engineering Chemistry Research*, 52(32), 11036–11044. https://doi.org/10.1021/ie401092f

Liu, L., Rong, H., Li, J., Tong, X. & Wang, Z. (2017) Synthesis of a hierarchical cobalt sulfide/cobalt basic salt nanocomposite via a vapor-phase hydrothermal method as an electrode material for supercapacitor. *New Journal of Chemistry*, 41(20), 12147–12152.

Lu, X., Huang, Z., Liang, Z., Li, Z., Yang, J., Wang, Y. & Wang, F. (2021) Co-precipitation of Cu and Zn in precipitation of struvite. *Science of the Total Environment*, 764, 144269.

Ma, Q.Y., Logan, T.J. & Traina, S.J. (1995) Lead immobilization from aqueous solutions and contaminated soils using phosphate rocks. *Environmental Science & Technology*, 29(4), 1118–1126. https://doi.org/10.1021/es00004a034

Magomya, A.M., Barminas, J.T. & Osemeahon, S.A. (2017) Assessment of metal-induced inhibition of soybean urease as a tool for measuring heavy metals in aqueous samples. *IOSR Journal of Applied Chemistry*, 10(6, Ver. II), 61–70.

Makinda, J., Kassim, K.A., Muhammed, A.S., Zango, M.U. & Gungat, L. (2023) Immobilization of heavy metal contaminants in mining waste through enzyme-induced calcite precipitation biocementation. *E3S Web of Conferences*, 464, 07001.

Manning, B.A. & Goldberg, S. (1996) Modeling competitive adsorption of arsenate with phosphate and molybdate on oxide minerals. *Soil Science Society of America Journal*, 60, 121–131. https://doi.org/10.2136/sssaj1996.03615995006000010020x

Mavromatis, V., González, A., Dietzel, M. & Schott, J. (2019) Zinc isotope fractionation during the inorganic precipitation of calcite – towards a new pH proxy. *Geochimica et Cosmochimica Acta*, 244, 99–112. https://doi.org/10.1016/j.gca.2018.09.005

Moghal, A.A.B., Lateef, M.A., Mohammed, S.A., Ahmad, M., Usman, A.R.A. & Almajed, A. (2020) Heavy metal immobilization studies and enhancement in geotechnical properties of cohesive soils by EICP technique. *Applied Sciences*, 10, 7568. https://doi.org/10.3390/app10217568

Nagarajan, A., Chen, Y., Raghavan, V., Goyette, B. & Rajagopal, R. (2024) Sustainable nutrient recovery through struvite precipitation from poultry and multi-substrate agricultural waste digestates. *Bioresource Technology Reports*, 27, 101924. https://doi.org/10.1016/j.biteb.2024.101924

Pan, H., Liu, X.Y., Tang, R. & Xu, H.Y. (2010) Mystery of the transformation from amorphous calcium phosphate to hydroxyapatite. *Chemical Communications*, 46(39), 7415–7417. https://doi.org/10.1039/C0CC02361D

Parigi, R., Chen, N., Liu, P., Ptacek, C.J. & Blowes, D.W. (2022) Mechanisms of Ni removal from contaminated groundwater by calcite using X-ray absorption spectroscopy and Ni isotope measurements. *Journal of Hazardous Materials*, 440, 129679. https://doi.org/10.1016/j.jhazmat.2022.129679

Park, J., Kim, E., Oh, S., Kim, H., Kim, S., Kim, Y.P. & Song, M. (2021) Contributions of ammonia to high concentrations of PM2.5 in an urban area. *Atmosphere*, 12(12), 1676. https://doi.org/10.3390/atmos12121676

Pastero, L., Costa, E., Bruno, M., Rubbo, M. & Aquilano, D. (2004) Morphology of calcite ($CaCO_3$) crystals growing from aqueous solutions in the presence of Li^+ ions: surface behavior of the {0001} form. *Crystal Growth & Design*, 4(3), 485–490. https://doi.org/10.1021/cg034217r

Powell, N., Shilton, A. & Chisti, Y. (2007) Total ammonia–nitrogen removal by ion exchange in oxidation ditch municipal wastewater treatment systems. *Journal of Environmental Engineering*, 133(1), 89–96.

Powell, K.J., Brown, P.L., Byrne, R.H., Gajda, T., Hefter, G., Leuz, A.K., Sjöberg, S. & Wanner, H. (2007) Chemical speciation of environmentally significant metals with inorganic ligands. Part 2: the Cu^{2+} + OH^-, Cl^-, CO_3^{2-}, SO_4^{2-}, and PO_4^{3-} systems. *Pure and Applied Chemistry*, 79(5), 895–950. https://doi.org/10.1351/pac200779050895

Reddy, G.N. & Prasad, M.N.V. (1990) Heavy metal-binding proteins/peptides: occurrence, structure, synthesis and functions. A review. *Environmental and Experimental Botany*, 30(3), 251–264. https://doi.org/10.1016/0098-8472(90)90024-Z

Renard, F., Putnis, C.V., Montes-Hernandez, G., Ruiz-Agudo, E., Hövelmann, J. & Sarret, G., 2015. Interactions of arsenic with calcite surfaces revealed by in situ nanoscale imaging. *Geochimica et Cosmochimica Acta*, 159, pp.61–79. https://doi.org/10.1016/j.gca.2015.03.025

Rivadeneyra, M., Martín-Algarra, A., Sánchez-Román, M. et al. (2010) Amorphous Ca-phosphate precursors for Ca-carbonate biominerals mediated by *Chromohalobacter marismortui*. *ISME Journal*, 4, 922–932. https://doi.org/10.1038/ismej.2010.17

Rouff, A.A. (2012) Sorption of chromium with struvite during phosphorus recovery. *Environmental Science & Technology*, 46(22), 12493–12501. https://doi.org/10.1021/es302296m

Rouff, A.A. & Juarez, K.M. (2014) Zinc interaction with struvite during and after mineral formation. *Environmental Science & Technology*, 48(11), 6342–6349. https://doi.org/10.1021/es500188t

Ryan, J.A., Zhang, P., Hesterberg, D., Chou, J. & Sayers, D.E. (2001) Formation of chloropyromorphite in a lead-contaminated soil amended with hydroxyapatite. *Environmental Science & Technology*, 35(18), 3798–3803. https://doi.org/10.1021/es010634l

Saidou, H., Korchef, A., Moussa, S.B. & Amor, M.B. (2015) Study of Cd^{2+}, Al^{3+}, and SO_4^{2-} ions influence on struvite precipitation from synthetic water by dissolved CO_2 degasification technique. *Open Journal of Inorganic Chemistry*, 5(3), 41–51.

Shannon, R.D. (1976) Revised effective ionic radii and systematic studies of interatomic distances in halides and chalcogenides. *Acta Crystallographica Section A*, 32(5), 751–767.

Shu, S., Yan, B., Ge, B., Li, S. & Meng, H. (2022) Factors affecting soybean crude urease extraction and biocementation via enzyme-induced carbonate precipitation (EICP) for soil improvement. *Energies*, 15(15), 5566. https://doi.org/10.3390/en15155566

Singh, N.A. (2017) Biomolecules for removal of heavy metal. *Recent Patents on Biotechnology*, 11(3), 197–203. https://doi.org/10.2174/1872208311666170223155019

Stocks-Fischer, S., Galinat, J.K. & Bang, S.S. (1999) Microbiological precipitation of $CaCO_3$. *Soil Biology and Biochemistry*, 31, 1563–1571.

Svane, S., Sigurdarson, J.J., Finkenwirth, F., Eitinger, T. & Karring, H. (2020) Inhibition of urease activity by different compounds provides insight into the modulation and association of bacterial nickel import and ureolysis. *Scientific Reports*, 10, 8503. https://doi.org/10.1038/s41598-020-65405-3

Takagi, S., Chow, L.C. & Ishikawa, K. (1998) Formation of hydroxyapatite in new calcium phosphate cements. *Biomaterials*, 19(17), 1593–1599. https://doi.org/10.1016/s0142-9612(97)00119-1

Tang, S., Dong, Z., Ke, X., Luo, J. & Li, J. (2021) Advances in biomineralization-inspired materials for hard tissue repair. *International Journal of Oral Science*, 13(1), 42. https://doi.org/10.1038/s41368-021-00134-1

Tang, C., Liu, Z., Peng, C., Chai, L.-Y., Kuroda, K., Okido, M. & Song, Y.-X. (2019) New insights into the interaction between heavy metals and struvite: struvite as platform for heterogeneous nucleation of heavy metal hydroxide. *Chemical Engineering Journal*, 365, 60–69. https://doi.org/10.1016/j.cej.2019.02.034

Tardif, S., Cipullo, S., Sø, H.U., Wragg, J., Holm, P.E., Coulon, F., Brandt, K.K. & Cave, M. (2019) Factors governing the solid phase distribution of Cr, Cu and As in contaminated soil after 40 years of ageing. *Science of the Total Environment*, 652, 744–754. https://doi.org/10.1016/j.scitotenv.2018.10.244

Torres-Aravena, Á.E., Duarte-Nass, C., Azócar, L., Mella-Herrera, R., Rivas, M. & Jeison, D. (2018) Can microbially induced calcite precipitation (MICP) through a ureolytic pathway be successfully applied for removing heavy metals from wastewaters? *Crystals*, 8(11), 438. https://doi.org/10.3390/cryst8110438

UN (2021) *International Year of Groundwater 2022: Global groundwater sustainability*. New York: United Nations.

Vandenbossche, M., Jimenez, M., Casetta, M. & Traisnel, M. (2015) Remediation of heavy metals by biomolecules: a review. *Critical Reviews in Environmental Science and Technology*, 45(15), 1644–1704. https://doi.org/10.1080/10643389.2014.966425

Wang, Y., Konstantinou, C., Tang, S. & Chen, H. (2023) Applications of microbial-induced carbonate precipitation: a state-of-the-art review. *Biogeotechnics*, 1(1), 100008. https://doi.org/10.1016/j.bgtech.2023.100008

Wang, Z., Chen, J., Cai, H. et al. (2021) Coprecipitation of metal ions into calcite: an estimation of partition coefficients based on field investigation. *Acta Geochimica*, 40, 67–77. https://doi.org/10.1007/s11631-020-00443-1

Wang, L., Ruiz-Agudo, E., Putnis, C.V., Menneken, M. & Putnis, A. (2012) Kinetics of calcium phosphate nucleation and growth on calcite: implications for predicting the fate of dissolved phosphate species in alkaline soils. *Environmental Science & Technology*, 46(2), 834–842.

Weiner, S. & Addadi, L. (2011) Crystallization pathways in biomineralization. *Annual Review of Materials Research*, 41, 21–40. https://doi.org/10.1146/annurev-matsci-062910-095803

Whiffin, V.S. (2004) *Microbial $CaCO_3$ precipitation for the production of biocement*. PhD thesis, Murdoch University.

Wilcox, S.M., Mulligan, C.N. & Neculita, C.M. (2024) Microbially induced calcium carbonate precipitation as a bioremediation technique for mining waste. *Toxics*, 12(2), 107. https://doi.org/10.3390/toxics12020107

Witek-Krowiak, A. & Reddy, D.H.K. (2013) Removal of microelemental Cr(III) and Cu(II) by using soybean meal waste – unusual isotherms and insights of binding mechanism. *Bioresource Technology*, 127, 350–357. https://doi.org/10.1016/j.biortech.2012.09.077

Yan, Y., Fang, Y., Verma, V., Li, J., Wang, Y., Yang, Y., Chen, F., Zhu, R., Wu, S., Hooper, T.J.N. & White, T. (2023) Phase evolution and arsenic immobilization of arsenate-bearing amorphous calcium phosphate. *Journal of Hazardous Materials*, 448, 130973. https://doi.org/10.1016/j.jhazmat.2023.130973

Yang, X., Wan, Y., Zheng, Y., He, F., Yue, Z., Huang, J., Wang, H., Ok, Y.S., Jiang, Y. & Gao, B. (2019) Surface functional groups of carbon-based adsorbents and their roles in the removal of heavy metals from aqueous solutions: a critical review. *Chemical Engineering Journal*, 366, 608–621. https://doi.org/10.1016/j.cej.2019.02.119

Yaashikaa, P.R., Palanivelu, J. & Hemavathy, R.V. (2024) Sustainable approaches for removing toxic heavy metal from contaminated water: a comprehensive review of bioremediation and biosorption techniques. *Chemosphere*, 357, 141933. https://doi.org/10.1016/j.chemosphere.2024.141933

Yu, X. et al. (2020) Review on potential uses, cementing process, mechanism and syntheses of phosphate cementitious materials by the microbial mineralization method. *Construction and Building Materials*, 260, 121113. https://doi.org/10.1016/j.conbuildmat.2020.121113

Yuan, H., Ru, M., Cong, W. & Wang, K. (2024) Ammonium nitrogen removal using natural zeolite in the process of enzyme-induced carbonate precipitation solidification for silty sand. *Journal of Water Process Engineering*, 64, 105713. https://doi.org/10.1016/j.jwpe.2024.105713

Xie, Y.X., Cheng, W.C., Wang, L., Wang, Y., Yu, J. & Yang, L. (2023) Biopolymer-assisted enzyme-induced carbonate precipitation for immobilizing Cu ions in aqueous solution and loess. *Environmental Science and Pollution Research*, 30, 116134–116146. https://doi.org/10.1007/s11356-023-30665-8

Xu, Y., Schwartz, F.W. & Traina, S.J. (1994) Sorption of Zn^{2+} and Cd^{2+} on hydroxyapatite surfaces. *Environmental Science & Technology*, 28(8), 1472–1480. https://doi.org/10.1021/es00057a015

Xu, Y. & Schwartz, F.W. (1994) Lead immobilization by hydroxyapatite in aqueous solutions. *Journal of Contaminant Hydrology*, 15(3), 187–206. https://doi.org/10.1016/0169-7722(94)90024-8

Zambelli, B., Musiani, F., Benini, S. & Ciurli, S. (2011) Chemistry of Ni^{2+} in urease: sensing, trafficking, and catalysis. *Accounts of Chemical Research*, 44(7), 520–530. https://doi.org/10.1021/ar200036c

Zeng, H., Jin, B., Xu, S., Han, L., Wang, J., Jia, H., Dapaah, M.F. & Cheng, L. (2025) Removal of copper, lead and cadmium from water through enzyme-induced carbonate precipitation by soybean urease. *Environmental Research*, 277, 121610. https://doi.org/10.1016/j.envres.2025.121610

Zeng, G., Wan, J., Huang, D., Hu, L., Huang, C., Cheng, M., Xue, W., Gong, X., Wang, R. & Jiang, D. (2017) Precipitation, adsorption and rhizosphere effect: the mechanisms for phosphate-induced Pb immobilization in soils—a review. *Journal of Hazardous Materials*, 339, 354–367. https://doi.org/10.1016/j.jhazmat.2017.06.036

Zhang, K. & Zhang, S. (2024) Feasibility study of applying enzyme-induced carbonate precipitation (EICP) without calcium source for remediation of lead-contaminated loess. *Buildings*, 14(6), 1810. https://doi.org/10.3390/buildings14061810

Zheng, L., Lin, H., Dong, Y., Li, B. & Lu, Y. (2023) A promising approach for simultaneous removal of ammonia and multiple heavy metals from landfill leachate by carbonate precipitating bacterium. *Journal of Hazardous Materials*, 456, 131662. https://doi.org/10.1016/j.jhazmat.2023.131662

Zhong, M., Liu, B., Zhang, L., Wang, J., Chen, J., Li, J., Liu, Y. & Ming, L. (2022) Experimental study on microbial induced calcium carbonate precipitation to enhance reservoir recovery. *Iranian Journal of Biotechnology*, 20(1), e3024. https://doi.org/10.30498/ijb.2021.279942.3024

Zhu, T. & Dittrich, M. (2016) Carbonate precipitation through microbial activities in natural environment, and their potential in biotechnology: a review. *Frontiers in Bioengineering and Biotechnology*, 4, 4. https://doi.org/10.3389/fbioe.2016.00004